Article

Not peer-reviewed version

Unbound Low-Energy Nucleons As Semiclassical Quantum Networks

Steven Charles Verrall * , Andrew Kaminsky , Kori Noelle Verrall , Isaac Ozolins , Emily Friederick , Andrew Otto , Peter Lynch , Kelly Susan Verrall , Ivan Ngian , Reagen McCormick , Pearl Scallon , Seth Schaffer , Stephanie San Juan

Posted Date: 14 May 2024

doi: 10.20944/preprints202405.0932.v1

Keywords: nucleon g-factor; Möbius band; fine-structure constant; quark charges; quark masses; W boson mass; proton charge radius; energetic causal sets; circular Unruh effect; intrinsic charm quarks

Preprints.org (www.preprints.org) | NOT PEER-REVIEWED | Posted: 14 May 2024 doi:10.20944/preprints202405.0932.v1

Article

Unbound Low-Energy Nucleons as Semiclassical Quantum Networks

Steven Verrall [1,*], Andrew Kaminsky [1,2,3], Kori N. Verrall [4], Isaac Ozolins [1,5], Emily Friederick [1], Andrew Otto [1,6], Peter Lynch [7], Kelly S. Verrall [8], Ivan Ngian [1], Reagen McCormick [1], Pearl Scallon [1], Seth Schaffer [1] and Stephanie San Juan [1]

1 Physics Department, University of Wisconsin at La Crosse, La Crosse, WI 54601, USA
2 Multistack, LLC, 1065 Maple Ave, Sparta, WI 54656, USA
3 Benchmark, 4065 Theurer Blvd, Winona, MN 55987, USA
4 La Crosse Aquinas High School, 315 11th St S, La Crosse, WI 54601, USA
5 ThermTech, Inc., 301 Travis Lane, Waukesha, WI 53189, USA
6 St. Croix Health, 235 State Street, St. Croix Falls, WI 54024, USA
7 School of Mathematics and Statistics, University College Dublin, Belfeld, Dublin 4, Ireland
8 Independent Researcher, La Crosse, WI 54601, USA
* Correspondence: sverrall@uwlax.edu; steven.verrall@gmail.com

Abstract: We propose that quarks and gluon flux tubes emerge from networks of standing vacuum waves. Each unbound nucleon, in its ground state, may be electromagnetically modeled as massless quantized charge on two pairs of orbiting arcs. Each charge arc is associated with a superposition of radially-oriented vacuum fundamental harmonics. These quantum superpositions of radial waves are coupled to nucleon mass-energy. The charge arcs orbit on the two surfaces of a spindle torus with polar charge-exclusion zones. These ground-state models of unbound nucleons may be interpreted as pairs of virtual Möbius bands. The optimal triangular Möbius band may explain proton uniqueness. These unbound proton and neutron models are shown to be precisely connected via a parameter dependent on neutron mass and the sum of the up and down bare quark masses. Due to this precise connection, and the relatively high experimental precision of proton magnetic moment, neutron magnetic moment is calculated about two orders of magnitude more precisely than the most accurate experiments to date. This quantum network-based approach to modeling unbound low-energy nucleons calculates several other measurable parameters.

Keywords: nucleon g-factor; Möbius band; fine-structure constant; quark charges; quark masses; W boson mass; proton charge radius; energetic causal sets; circular Unruh effect; intrinsic charm quarks

---

1. Introduction

Energetic unbound protons and neutrons are extremely complex structures [1,2] and their structures are still not fully understood [3,4]. However, at least at low energies, they appear to precisely maintain several important parameters. These include mass, net charge, spin, isospin, parity, magnetic moment, and rms charge radius. While free neutrons spontaneously decay with a mean lifetime of a little under 15 minutes [5], free protons possess such a stable ground state that free-proton decay has never been observed.

Quantum field theory (QFT) is arguably the most successful scientific theory developed to date [6]. It has produced the highly-precise Standard Model of particle physics [7]. However several Standard Model parameters must be experimentally determined. A reason why QFT, sans experiment, may be incapable of precisely explaining the values of certain particle properties could be because operators are applied to create and annihilate particles [6,8]. This conceptual shortcut mathematically precludes potential physical mechanisms that create and annihilate mass and charge.

This paper develops an argument that quantum networks of interfering virtual vacuum momenta continually regenerate the mass and charge of unbound nucleons when in their ground state. These

Preprints.org (www.preprints.org) | NOT PEER-REVIEWED | Posted: 14 May 2024 doi:10.20944/preprints202405.0932.v1

are called unbound ground-state quantum vortex (GSQV) nucleon models. As with Reference [9], during nucleon-antinucleon pair production, it is assumed that one real spin-1 photon splits into two virtual circularly-polarized spin-half photon vortices. When in its ground state, each unbound spin-half nucleon's mass energy is assumed to be generated from its toroidal vortex component via the combined zitterbewegung and circular Unruh effects [9]. The circular polarization of a toroidally revolving virtual photon results in a poloidal vortex component that Reference [9] assumes generates charge. This paper goes further by mathematically developing a mechanism via which unbound GSQV nucleon charge is generated and maintained via twin poloidal circulations.

In each unbound GSQV nucleon, the combined toroidal and poloidal actions are proposed to form twin virtual Möbius bands with length set to unbound nucleon Compton wavelength. The width of each virtual Möbius band is set to half the wavelength of an ensemble of quantized virtual vacuum momenta. In an unbound GSQV proton, each virtual Möbius band is proposed to be optimal in the sense of being maximally confined given its length [10–13]. This maximal confinement is interpreted as a state of minimum energy. By the same metric, an unbound GSQV neutron's virtual Möbius bands are suboptimal. This may explain why neutron mass energy necessarily exceeds proton mass energy. Importantly, these unbound GSQV nucleon models are purely field-based and therefore avoid the fundamental dilemmas of point-like particles [8]. This proposed conceptual framework may align with energetic causal set theory–where spacetime emerges from momentum space and the conservation of energy-momentum [14–21].

The modeling presented in this paper is proposed to add to QFT without replacing any of its long-established aspects. The goal is to enhance established QFT by explaining the creation and maintenance of nucleon mass, charge, and magnetic moment while in the ground state. This paper in no way doubts the fundamental validity of quantum chromodynamics (QCD) [22,23]. Nucleon modeling via lattice QCD may be conceptually correct, but is extremely computationally expensive [24], and it is not known how bare current quarks transition into dressed constituent quarks [25,26]. The precision of chiral effective field theory (EFT) [27] has generally been good, but recent discrepancies have emerged at the lowest energies [28–33]. This paper offers an alternative approach to modeling unbound ground-state nucleons that seamlessly merges with chiral EFT [27] and lattice QCD [24,34] at higher energies.

2. Materials and Methods

All calculations use publicly available CODATA [35,36] and Particle Data Group [5] data. All calculations were performed using the supplied Excel file. All mathematical manipulations were performed by the authors.

3. Results

3.1. Nucleon Properties from Quantum Networks

Recent photon-based nucleon models, conceptually similar to those presented in this paper, have been proposed [9,37–39]. However, References [37], [38], and [39] propose models that directly conflict with established QCD. In contrast this paper, as with Reference [9], fully accepts established QCD. As with Reference [9], this paper also conceptually explains the origin of quarks, gluons, color charge, and virtual pion clouds. This paper adds an explanation for intrinsic charm quarks [1,40–50].

This paper proposes that any unbound nucleon, in its lowest energy (ground) state, is a completely coherent self-synchronizing structure. At energies above the ground state, these unbound nucleon structures are proposed to transform into the quarks and gluons of established QCD theory. Therefore, at higher energies, there should be no conflict with the established chiral EFT [27] and lattice QCD [24,34] models. The unbound nucleon models developed in this paper may help resolve recently-discovered discrepancies occurring at the lowest energies [28–33]. Section 3.1.3 shows that up, charm, and top quark charge appears to depend only on Planck charge, the proportionate area of an unbound GSQV proton's charge-exclusion zone, and π. Section 3.2 applies these quantum network-based models to calculate several parameters related to quarks and neutron decay. The proton models developed both in this paper and Reference [9] are statistically consistent with a recent experimental estimate of proton polar charge radius [51].

As with Reference [9], this paper proposes that the properties of an unbound ground-state nucleon's measured projection can be derived from those of a hypothetical revolving circularly-polarized virtual photon. Such a virtual photon is proposed to propagate via both toroidally and poloidally revolving virtual electromagnetic fields. The virtual photon's energy is assumed to be identical to nucleon mass energy. The unbound nucleon's mass energy is proposed to be a quantized manifestation of the circular Unruh energy [52–64] of an uncharged zitterbewegung fermion [9]. It is reasonable to assume that the Unruh effect is fundamentally local [65]. Reference [9] explains mathematically how such an uncharged zitterbewegung fermion could generate a gravitational field by concentrating circular Unruh energy and curving spacetime [66].

The proposed central uncharged zitterbewegung fermion is not shown in this paper's figures. Following Reference [9], it's radius is $\lambda_N/4\pi$, where λ_N is unbound nucleon Compton wavelength. This puts it well inside each massless charge arc described in this paper. Recent experimental evidence has shown proton rms mass radius to be substantially smaller than proton rms charge radius [67]. The experimental analysis shows that proton rms mass radius tends to decrease at lower energies [67]. Hansson has argued [68], that at low momentum transfers, the quarks and gluons of QCD cannot be defined and thus do not really exist within a proton. As with Reference [9], this paper proposes that quarks and gluons do not exist in a nucleon's absolute ground state, but that gluon energy and quark relativistic energy are sourced from the central zitterbewegung fermion's mass energy at energies above the ground state. Therefore, as nucleon energy increases, the nucleon models developed this paper are fully consistent with the increase in proton rms mass radius experimentally determined by Reference [67].

In 1989, Reference [69] reported vortex solutions of the Maxwell-Bloch equations and described the concept of optical vortices. Such vortices involve both toroidal and poloidal motion [69–72]. This paper models unbound nucleons as virtual optical vortices of much higher energy, and on a much smaller scale, than those produced by non-nuclear optics experiments. This is called the zitterbewegung effect [8,9,37–39,73–81], where toroidal motion is associated with quantum mechanical spin. This paper, and Reference [9], associate poloidal motion with isospin [82,83] and charge. Recent experimental evidence [84–87], supports the concept of the zitterbewegung effect being due to stable intrinsic high frequency oscillations.

During nucleon-antinucleon pair production, this paper assumes that a virtual photon's toroidal motion generates nucleon mass energy. It is also assumed that such a virtual photon's poloidal motion generates nucleon charge. Such charge generation was described conceptually, but not mathematically, in Reference [9]. This paper mathematically develops a mechanism via which nucleon charge is generated and maintained. This mechanism features multiple charge arcs–each assumed to maintain its charge. These are shown in Figures 1, 2, 3, and 4, where e represents quantized electronic charge. The application of higher symmetries in QFT has shown that evolving one-dimensional charge strings can conserve charge on their world sheets [88,89].

Preprints.org (www.preprints.org) | NOT PEER-REVIEWED | Posted: 14 May 2024 doi:10.20944/preprints202405.0932.v1

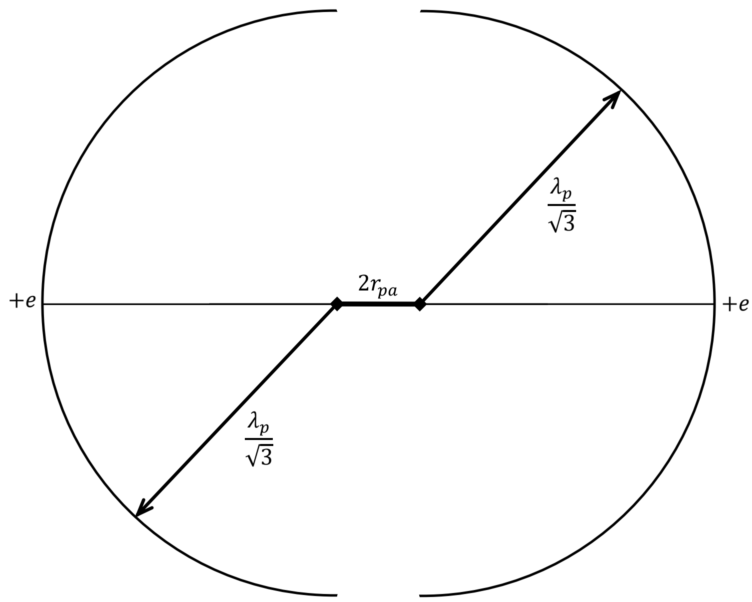

Figure 1. Outer charge arcs of the unbound GSQV proton, where λ_p is proton Compton wavelength and $r_{pa} = \lambda_p(1/\sqrt{3} - 1/2)$. Each arc is of radius $R_p = \lambda_p/\sqrt{3}$ and extends for π radians. An ensemble of virtual vacuum standing waves connects each arc to its radial center. The charge equator revolves toroidally at light speed.

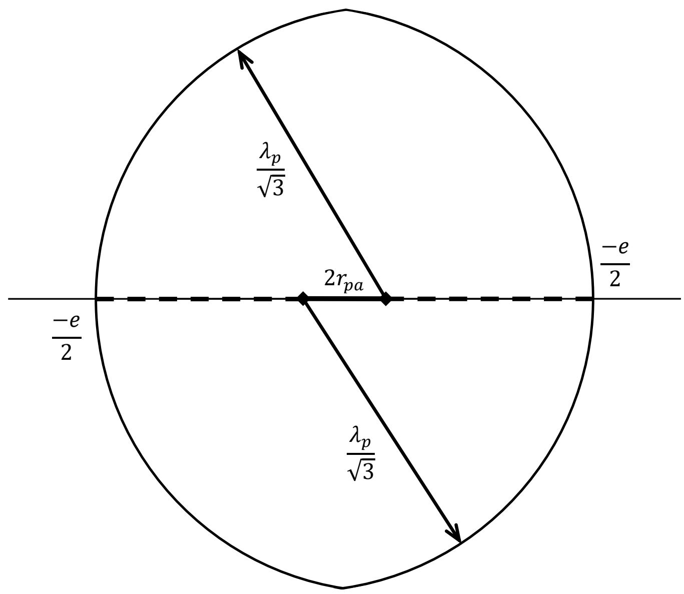

Figure 2. Inner charge arcs of the unbound GSQV proton, where λ_p is proton Compton wavelength and $r_{pa} = \lambda_p(1/\sqrt{3} - 1/2)$. Each arc is of radius $R_p = \lambda_p/\sqrt{3}$ and extends for $2\phi_{pl} = 2\cos^{-1}(1 - \sqrt{3}/2)$ radians. An ensemble of virtual vacuum standing waves connects each arc to its radial center. The horizontal line represents the equatorial diameter formed by the outer charge arcs in Figure 1. The distance between the equatorial points of the inner charge arcs is λ_p. They are connected by virtual vacuum standing waves and revolve toroidally at light speed. The inner and outer R_p vectors are poloidally phase locked and occasionally overlap in two places almost simultaneously, as indicated by the dashed lines.

Preprints.org (www.preprints.org) | NOT PEER-REVIEWED | Posted: 14 May 2024 doi:10.20944/preprints202405.0932.v1

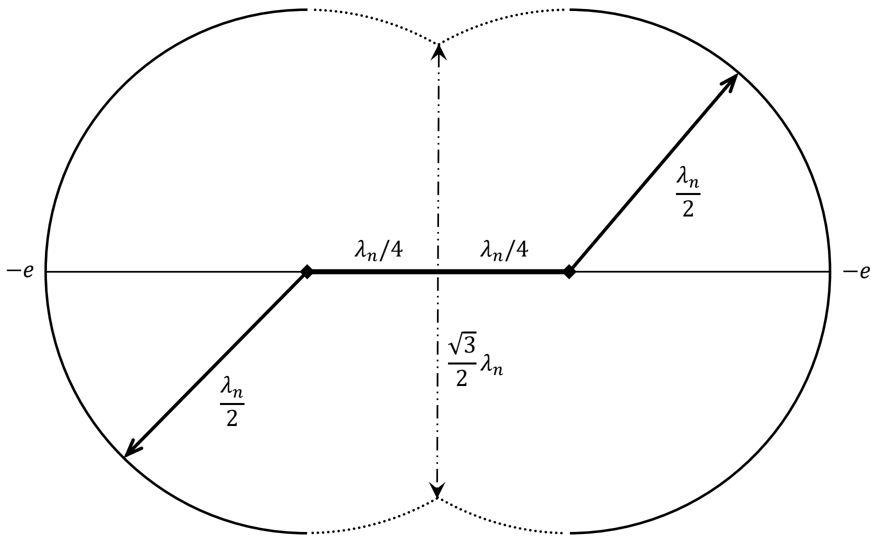

Figure 3. Outer charge arcs of the unbound GSQV neutron, where λ_n is neutron Compton wavelength. The solid curves, of radius $R_n = \lambda_n/2$ and extending for π radians, are each charged $-e$. Each dotted arc is uncharged and extends for $\pi/6$ radians. An ensemble of virtual vacuum standing waves connects each arc to its radial center. The two radial centers are $\lambda_n/2$ apart. The charge equator revolves toroidally at light speed. The two polar points are separated by $\sqrt{3}\lambda_n/2$. Figure 4 shows that these two polar points are the ends of arcs of positive charge.

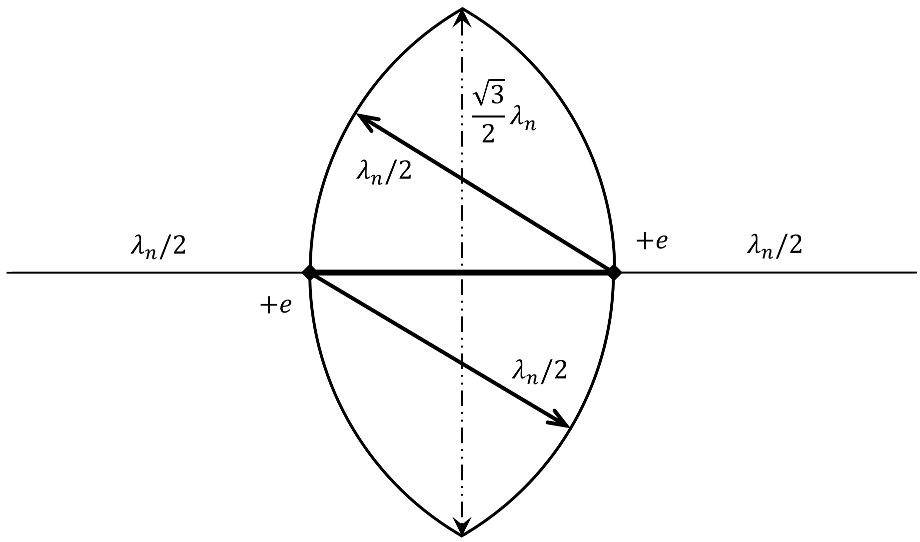

Figure 4. Inner charge arcs of the unbound GSQV neutron, where λ_n is neutron Compton wavelength. Each charge arc is of radius $R_n = \lambda_n/2$, extends for $2\phi_{nl} = 2\pi/3$ radians, and is charged $+e$. An ensemble of virtual vacuum standing waves connects each arc to its radial center. The two radial centers are connected by a virtual vacuum standing wave that revolves toroidally at light speed. The horizontal line represents the equatorial diameter formed by the outer charge arcs in Figure 3. The inner and outer R_n vectors are poloidally phase locked and thus cannot overlap. The two polar points, separated by $\sqrt{3}\lambda_n/2$, are connected by virtual vacuum standing waves.

 doi:10.20944/preprints202405.0932.v1

When in its ground state, this paper assumes that nucleon charge and mass are coupled and continually regenerate each other. This assumption may align with energetic causal set theory–where spacetime emerges from momentum space and the conservation of energy-momentum [14–21]. For each charge arc, this coupling may be represented in the form of a virtual Möbius band. Each charge arc is assumed to be regenerated by half a poloidal turn, at radius R_N, each zitterbewegung cycle. For the proton, $R_N = R_p = \lambda_p/\sqrt{3}$, where λ_p is proton Compton wavelength. For the neutron, $R_N = R_n = \lambda_n/2$, where λ_n is neutron Compton wavelength. Since unbound ground-state nucleons are spin-half particles, each zitterbewegung cycle involves two revolutions of the central zitterbewegung fermion [9]. A zitterbewegung cycle may be characterized by Compton wavelength, λ_N, and Compton frequency, $f_N = c/\lambda_N$, where c is the speed of light.

Figure 5 illustrates the virtual Möbius bands of unbound GSQV nucleons. The aspect ratio of each virtual Möbius band in an unbound GSQV neutron is $\lambda_n/R_n = 2$. The aspect ratio of each virtual Möbius band in an unbound GSQV proton is $\lambda_p/R_p = \sqrt{3}$. Note that $2 > \sqrt{3}$ and that $\sqrt{3}$ is the minimum possible aspect ratio of a smooth Möbius band [10–13]. This implies that the geometry of an unbound GSQV proton may be optimal. This may explain why free protons do not decay. Appendix A discusses supplementary details of the optimal Möbius band.

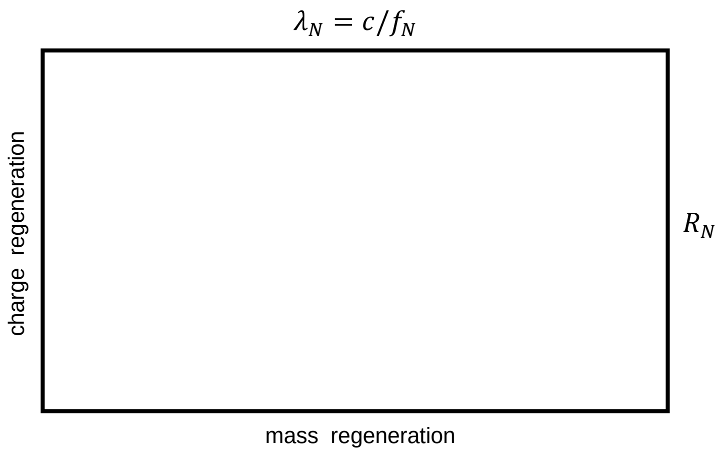

Figure 5. Coupled charge and mass regeneration may be described in terms of virtual Möbius bands. To form a Möbius band, the sides of length R_N are joined following a half turn.

The proposed charge generation and regeneration mechanism involves interfering standing waves of vacuum momenta. The massless charge arcs of the proposed unbound GSQV nucleon models are shown in Figures 1, 2, 3, and 4. Each charge arc is proposed to be associated with an ensemble of vacuum standing waves continually reflecting between all points on each charge arc and its radial center. These standing waves are proposed to be fundamental harmonics. Sections 3.1.3 and 3.1.5 propose that arc charge is continually regenerated via mass-energy coupling.

The inner charge arcs of the proposed GSQV proton are shown in Figure 2. Section 3.1.2 proposes that the charge arc standing-wave ensembles, of all four charge arcs shown in Figures 1 and 2, interfere with another standing wave connecting the equatorial points of the two charge arcs in Figure 2. This equatorial standing wave is consistent with quantum electrodynamics (QED), where electric force is carried by virtual photons [90–92]. Section 3.1.2 shows that the rms value of the sum of the fundamental equatorial harmonic, and the fundamental proton charge-arc harmonic, is the second equatorial harmonic. As with Reference [9], the wavelength of this second equatorial harmonic is set to the proton Compton wavelength. This inner-arc equatorial separation distance is the key to calculating proton magnetic moment and charge radius from proton mass [9].

The inner charge arcs of the proposed GSQV neutron are shown in Figure 4. A standing wave is proposed to connect the equatorial points of the two charge arcs in Figure 4. This equatorial standing wave is consistent with QED, where electric force is carried by virtual photons [90–92]. The wavelength

Preprints.org (www.preprints.org) | NOT PEER-REVIEWED | Posted: 14 May 2024 doi:10.20944/preprints202405.0932.v1

of this fundamental equatorial harmonic is set to the neutron Compton wavelength. This inner-arc equatorial separation distance is the key to calculating neutron magnetic moment.

Section 3.1.2 proposes that the charge arc standing-wave ensembles, of all four charge arcs shown in Figures 3 and 4, interfere with another standing wave connecting the poles of the two charge arcs in Figure 4. This polar standing wave is consistent with QED, where electric force is carried by virtual photons [90–92]. Section 3.1.2 shows that the rms value of the sum of the fundamental polar harmonic, and the fundamental neutron charge-arc harmonic, is the second polar harmonic.

A crucial difference between the charge arcs of the GSQV proton and GSQV neutron is that the proton's inner charge arcs are quantized with magnitude $e/2$ instead of e. In Section 3.1.3, Equation (31) models charge arc regeneration as a virtual poliodal flow. Charge generation via the poloidal overturning of virtual electromagnetic fields was subjectively proposed in Reference [9]. As shown in Figure 6, this paper proposes that virtual poloidal flow is split between two paths of equal magnitude where charge regeneration switches off in the GSQV proton's polar regions. This split flow does not occur in the GSQV neutron's polar regions. This difference may explain why the GSQV proton's inner charge arcs are of half the magnitude of the GSQV neutron's inner charge arcs. Because the equatorial points of all GSQV charge arcs circulate at light speed, the inner charge arcs rotate at a higher frequency than do the outer charge arcs. This necessarily causes a general step discontinuity, in the direction of virtual poloidal flow, at the transition point between an uncharged polar arc and a charged inner arc.

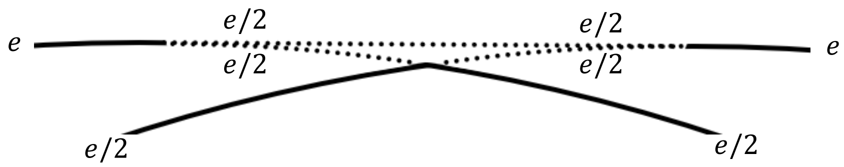

Figure 6. In the unbound GSQV proton's polar regions, virtual poloidal flow splits into two paths of equal magnitude. Dotted paths are uncharged. The revolving outer charge arcs are connected via a line that forms an uncharged virtual flat cap.

It will be assumed, that in the ground-state orbital of a ground-state proton, an electron or muon spin combines with the proton spin into a singlet state. Key evidence of this is the 21 cm hydrogen line observed in the galactic radio spectrum [93–95]. This implies that a ground-state electron or muon orbital magnetically interacts with a ground-state proton in such a way that it appears to possess the properties of the proton model projection presented in this paper. This assumption is used in Section 3.3.5 to estimate proton polar radius, consistent with a recent experimental result [51]. Section 3.3.5 also calculates an effective proton charge radius consistent with the 2022 recommended Particle Data Group proton rms charge radius range, $r_p = 0.8409(4)$ fm [5].

It will be assumed that an external magnetic field will cause the nucleon models, developed in this paper, to undergo Larmor precession [96–99]. A nucleon's gyromagnetic ratio, called its g-factor, directly depends on Larmor precession frequency [96–99]. However, nucleon g-factor is independent of Larmor precession angle [96–99]. Therefore the nucleon models, developed in this paper, will be assumed to be in the superposition of all possible precession angles. This may be described by a spherically-symmetric Bloch sphere [96,99].

3.1.1. Ground-State Quantum Vortex Neutron Model

An unbound ground-state neutron model is developed following a similar rationale to the development of the refined GSQV proton model in Reference [9]. An unbound GSQV neutron is constructed from four rotating charge arcs, as shown in Figures 3 and 4. The charge on each arc is quantized as the elementary charge, $\pm e$.

Preprints.org (www.preprints.org) | NOT PEER-REVIEWED | Posted: 14 May 2024 doi:10.20944/preprints202405.0932.v1

It is clear from Panel (a) of Figure 7 that this proposed neutron model contains three times as much positive charge, and three times as much negative charge, as that needed to form the neutron's valence quarks. However the minimally excited GSQV proton model, shown in Panel (b) of Figure 7 and initially developed in Reference [9], includes a virtual up sea quark ($+2e/3$ charge) and a virtual antiup sea quark ($-2e/3$ charge). These virtual sea quarks are assumed to initiate a proton's virtual pion cloud. Note that up and antiup quarks have approximately half the mass energy of down and antidown quarks. Therefore, an up-antiup quark pair represents a lower energy state than would a down-antidown quark pair. The GSQV neutron model, developed here, includes two pairs of virtual up-antiup sea quarks assumed to initiate a neutron's virtual pion cloud.

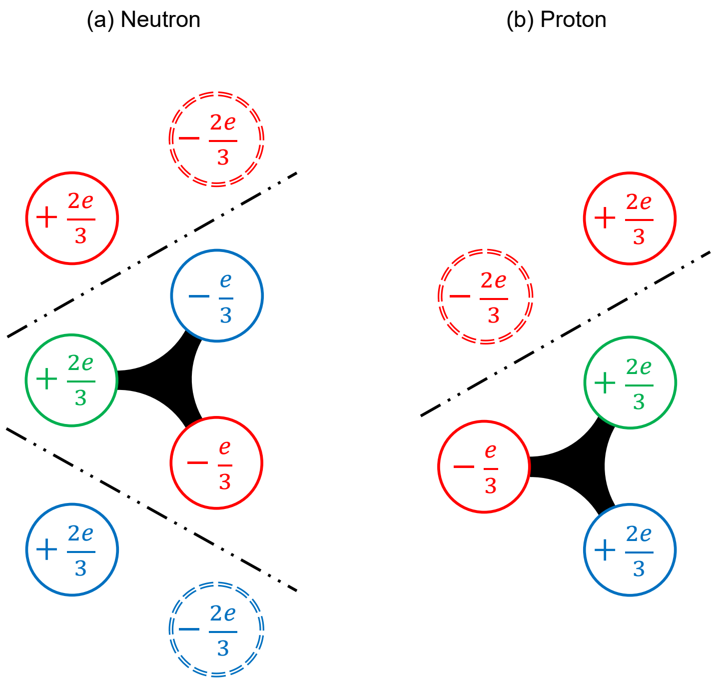

Figure 7. Minimally excited unbound GSQV nucleons. Each circle represents a quark. Dashed outlines represent anticolors. Gluons are continually exchanging color charge. (a), The three quarks in the left-hand column transition from the two inner $+e$ charge arcs of the GSQV neutron. These momentarily form a color-neutral quark triplet. The four quarks in the right-hand column transition from the two outer $-e$ charge arcs of the GSQV neutron. These momentarily form a color-neutral quark quartet. The three quarks between the dashed lines connect via gluon flux tubes to form the neutron's color-neutral valence quark triplet. (**b**), The two quarks in the left-hand column transition from the two inner $-e/2$ charge arcs of the GSQV proton. These momentarily form a color-neutral quark doublet. The three quarks in the right-hand column transition from the two outer $+e$ charge arcs of the GSQV proton. These momentarily form a color-neutral quark triplet. The three quarks below the dashed line connect via gluon flux tubes to form the proton's color-neutral valence quark triplet.

The Gerasimov-Drell-Hearn (GDH) sum rule [28,100–106], initially developed in the 1960s, relates the proton and neutron anomalous magnetic moments. The GDH sum rule involves two adjustable parameters that may be calculated–to high precision–from nucleon masses, nucleon magnetic moments, and the fine-structure constant. Experimental verification of the GDH sum rule parameters has only recently been attained [28,105].

Recent analysis shows that single-pion photoproduction off the nucleon is the dominant contribution to the GDH sum rule [106]. Reference [106] found that non-single-pion photoproduction off the proton amounts to about 10%, whereas non-single-pion photoproduction off the neutron

Preprints.org (www.preprints.org) | NOT PEER-REVIEWED | Posted: 14 May 2024 doi:10.20944/preprints202405.0932.v1

amounts to about 44%. This large difference may be partly explained by the minimally excited GSQV neutron containing twice as many virtual sea quarks as the minimally excited GSQV proton. The quarks above and below the dashed lines in Panel (a) of Figure 7, and above the dashed line in Panel (b) of Figure 7, may initiate pion production upon sufficient excitation. Therefore, Reference [106] provides experimental support for the GSQV neutron model plausibly containing two $+e$ and two $-e$ charge arcs.

In this paper, c is the speed of light, h is Planck's constant, and $\hbar = h/2\pi$ is the reduced Planck constant. As in Reference [9], proton zitterbewegung radius is defined as

$$r_{pz} = \frac{\hbar}{2m_p c} = \frac{\lambda_p}{4\pi}, \tag{1}$$

where $m_p = 1.67262192369(51) \times 10^{-27}$ kg is proton mass [35,36] and λ_p is proton Compton wavelength. Neutron Compton wavelength is defined as

$$\lambda_n = \frac{h}{m_n c}, \tag{2}$$

where $m_n = 1.67492749804(95) \times 10^{-27}$ kg is neutron mass [35,36]. Based on the refined GSQV proton model, developed in Reference [9], and Figures 3 and Figure 4 in this paper, neutron magnetic moment will be approximated by

$$\mu_n = \left(\frac{2V_{ni}}{(R_n - r_{na})^2} - \frac{2V_{no}}{(1 - Q_{nex})(R_n + r_{na})^2} \right) \frac{\mu_N}{4\pi r_{pz}}, \tag{3}$$

where V_{ni} is the lemon volume formed by rotating the neutron's two inner charge arcs about the neutron center, V_{no} is the apple volume formed by rotating the neutron's two outer charge arcs–plus uncharged extensions–about the neutron center, Q_{nex} is the uncharged proportion of the neutron's outer (apple) surface,

$$R_n = \frac{\lambda_n}{2}, \text{ and } r_{na} = \frac{\lambda_n}{4}. \tag{4}$$

Following Reference [9], define

$$\phi_{nl} = \cos^{-1}\left(\frac{r_{na}}{R_n}\right) = \cos^{-1}\left(\frac{1}{2}\right) = \frac{\pi}{3} \tag{5}$$

and

$$\phi_{na} = \pi - \phi_{nl} = \frac{2\pi}{3}. \tag{6}$$

Following the Appendix of Reference [9],

$$V_{ni} = \tfrac{4}{3}\pi R_n^3 \left[\sin^3\phi_{nl} - \tfrac{3}{4}\cos\phi_{nl}(2\phi_{nl} - \sin 2\phi_{nl})\right] = \frac{\pi\lambda_n^3}{96}\left(9\sqrt{3} - 4\pi\right) \tag{7}$$

and

$$V_{no} = \tfrac{4}{3}\pi R_n^3 \left[\sin^3\phi_{na} - \tfrac{3}{4}\cos\phi_{na}(2\phi_{na} - \sin 2\phi_{na})\right] = \frac{\pi\lambda_n^3}{96}\left(9\sqrt{3} + 8\pi\right). \tag{8}$$

Preprints.org (www.preprints.org) | NOT PEER-REVIEWED | Posted: 14 May 2024 doi:10.20944/preprints202405.0932.v1

Also following the Appendix of Reference [9], the charged proportion of the neutron's outer (apple) surface, $(1 - Q_{nex})$, will be the area of the surface of revolution formed by the outer charge arcs divided by the apple surface area:

$$1 - Q_{nex} = \frac{2\pi^2 R_n \left(r_{na} + \frac{2R_n}{\pi}\right)}{4\pi R_n^2 \left(\sin\phi_{na} - \phi_{na}\cos\phi_{na}\right)} = \frac{1 + \frac{\pi}{4}}{\frac{\sqrt{3}}{2} + \frac{\pi}{3}} = \frac{3(4+\pi)}{2\left(3\sqrt{3} + 2\pi\right)}. \tag{9}$$

Substituting Equations (4), (7), (8), and (9) into Equation (3) yields

$$\mu_n = \left[9\sqrt{3} - 4\pi - \frac{2\left(9\sqrt{3} + 8\pi\right)\left(3\sqrt{3} + 2\pi\right)}{27(4+\pi)}\right] \frac{\lambda_n\, \mu_N}{12 r_{pz}}. \tag{10}$$

Substituting Equations (1) and (2) into Equation (10) and simplifying,

$$\mu_n = \left[\frac{53\sqrt{3}}{36} - 4 - \frac{35\pi}{27} + \frac{3}{\pi}\left(3\sqrt{3} - \frac{1}{2}\right)\right] \frac{4\pi^2}{3(4+\pi)} \frac{m_p}{m_n}\, \mu_N \approx -1.91000\, \mu_N, \tag{11}$$

which is about 0.16% less negative than the 2018 CODATA value [35,36] displayed later in this section as Equation (23). Note that the m_p/m_n factor, in Equation (11), is due to the convention of defining the nuclear magneton, μ_N, in terms of the proton mass. If the nuclear magneton was instead defined in terms of the neutron mass, the form of Equation (11) would imply a neutron g-factor independent of the nucleon masses.

Since the ratio of proton to neutron mass is close to unity,

$$\mu_n \approx \left[\frac{53\sqrt{3}}{36} - 4 - \frac{35\pi}{27} + \frac{3}{\pi}\left(3\sqrt{3} - \frac{1}{2}\right)\right] \frac{4\pi^2}{3(4+\pi)}\, \mu_N \approx -1.91263\, \mu_N, \tag{12}$$

which is more than 7 times closer, than Equation (11), to the 2018 CODATA value [35,36] displayed later in this section as Equation (23). The surprising precision of Equation (12) may provide insights into the electron capture process of a proton-rich nucleus [107–109]. In an unstable proton-rich nucleus, suppose that the most loosely-bound proton experiences electron capture via the weak interaction [110]. Suppose that this process has the effect of the loosely-bound proton absorbing the former electron's charge, via a W boson, but not its mass, m_e. The weak interaction is addressed in detail in Section 3.2. During electron capture, suppose the former electron's mass energy cannot primarily be incorporated into the mass of the former proton. Energy dissipation pathways are therefore needed to facilitate the electron capture process. This may help explain the very low probabilities for neutral hydrogen and molecular hydrogen to undergo electron capture in extremely low-energy environments.

Suppose, that following the weak interaction [110], this loosely-bound former proton has the charge structure implied by Equations (3) and (10)–(12). Modifying Equation (11), if the mass of this loosely-bound former proton is close to $0.39717 m_e$ less than that of an unbound proton, its magnetic moment will closely resemble that of an unbound neutron:

$$\left[\frac{53\sqrt{3}}{36} - 4 - \frac{35\pi}{27} + \frac{3}{\pi}\left(3\sqrt{3} - \frac{1}{2}\right)\right] \frac{4\pi^2}{3(4+\pi)} \frac{m_p}{(m_p - 0.39717 m_e)}\, \mu_N \approx \mu_n. \tag{13}$$

The experimentally determined value of μ_n is displayed later in this section as Equation (23). This mass defect can be attributed to a relatively minor nuclear binding energy [111], which is consistent with a loosely-bound nucleon. Being electrically neutral, and possessing a substantial magnetic moment, this new nuclear neutron should be magnetically attracted to nearby nucleons and bind relatively strongly to the nucleus. Therefore, neutron binding may be initiated by semiclassical magnetic forces.

Preprints.org (www.preprints.org) | NOT PEER-REVIEWED | Posted: 14 May 2024 doi:10.20944/preprints202405.0932.v1

Evaluating the Equation (12) terms in the square parentheses,

$$\frac{53\sqrt{3}}{36} - 4 - \frac{35\pi}{27} + \frac{3}{\pi}\left(3\sqrt{3} - \tfrac{1}{2}\right) \approx -1.037976 \approx -\frac{\pi}{3}. \tag{14}$$

Substituting $-\pi/3$ for the square-parentheses terms in Equation (12) yields

$$\mu_n \approx \frac{-4\pi^3}{9(4+\pi)}\,\mu_N = -\left(\tfrac{2}{3}\right)^2 \frac{\pi^3}{(4+\pi)}\,\mu_N = -\left(\frac{q_u}{e}\right)^2 \frac{\pi^3}{(4+\pi)}\,\mu_N \approx -1.9296\,\mu_N, \tag{15}$$

where q_u is the charge of an up, charm, or top quark. These compact equations offer only 2-digit precision. However, their precision improves to 5 digits if the number 4, in the denominator, is replaced by $\sqrt{33/2}$:

$$\mu_n \approx -\left(\tfrac{2}{3}\right)^2 \frac{\pi^3}{\left(\sqrt{\frac{33}{2}}+\pi\right)}\,\mu_N = -\left(\frac{q_u}{e}\right)^2 \frac{\pi^3}{\left(\sqrt{\frac{33}{2}}+\pi\right)}\,\mu_N \approx -1.913008\,\mu_N. \tag{16}$$

While no rationale is offered to support the quantity $\sqrt{33/2}$, it is surprising that an equation involving just one 2-digit numeral can calculate an experimentally deterimined quantity to 5-digit precision.

Apart from the polar charge-exclusion zones on the GSQV neutron's outer apple-shaped charge surface, Equations (3) and (10)–(13) assume a direction-independent steradian charge distribution. This was a key assumption applied when developing the GSQV proton model in Reference [9]. This assumption implies that the linear charge density, along each charge arc, depends only on distance from nucleon center. This results in a non-uniform linear charge density along each charge arc.

It will now be assumed that each charge arc's linear charge density is slightly less non-uniform due to internal self-interaction that tends toward evening out charge distribution. This will not lead to a measurable electric quadrupole moment. This is because Larmor precession would still result in a uniform steradian charge distribution in the form of a Bloch sphere [96–99]. This slight charge redistribution will slightly change the magnetic moment contributed by each charge surface formed by the toroidally rotating charge arcs.

The neutron's inner positively-charged lemon-shaped surface will be assumed to redistribute via a slight poleward migration. Since the magnetic moment of a current loop depends on loop cross-sectional area, the neutron's inner positively-charged surface will now contribute a slightly smaller positive magnetic moment. Equation (3) will be modified by dividing the first term by $(1+\delta_n)$, where δ_n is dimensionless, positive, and much smaller than 1. Similarly, the neutron's outer negatively-charged surface will be assumed to redistribute via a slight equatorial migration. The neutron's outer negatively-charged surface will now contribute a slightly larger negative magnetic moment. Equation (3) will be modified by dividing the second term by $(1-\delta_n)$. An alternative implementation of adjustable parameter, δ_n, would be to multiply the first term of Equation (3) by $(1-\delta_n)$ and to divide the second term of Equation (3) by $(1+\delta_n)$. This alternative was not selected because it results in a larger δ_n value.

Therefore, a precise calculation of GSQV neutron magnetic moment may be obtained from

$$\mu_n = \left(\frac{2V_{ni}}{(1+\delta_n)(R_n - r_{na})^2} - \frac{2V_{no}}{(1-\delta_n)(1-Q_{nex})(R_n + r_{na})^2}\right)\frac{\mu_N}{4\pi r_{pz}}. \tag{17}$$

Substituting Equation (4) into Equation (17) yields

$$\mu_n = \left(\frac{V_{ni}}{(1+\delta_n)} - \frac{V_{no}}{9(1-\delta_n)(1-Q_{nex})}\right)\frac{8}{\pi\lambda_n^2 r_{pz}}\mu_N. \tag{18}$$

Preprints.org (www.preprints.org) | NOT PEER-REVIEWED | Posted: 14 May 2024 doi:10.20944/preprints202405.0932.v1

This equation may be solved for δ_n by collecting terms to form a quadratic equation in terms of δ_n:

$$a\delta_n^2 + b\delta_n + c = 0, \tag{19}$$

where

$$a = -9\pi(1 - Q_{nex})\lambda_n^2 r_{pz}\frac{\mu_n}{\mu_N}, \tag{20}$$

$$b = 72(1 - Q_{nex})V_{ni} + 8V_{no}, \tag{21}$$

and

$$c = 16V_{no} - a - b. \tag{22}$$

Using the 2018 CODATA value [35,36],

$$\mu_n = -1.91304273(45)\ \mu_N, \tag{23}$$

and applying the quadratic formula yields

$$\delta_n = \frac{-b \pm \sqrt{b^2 - 4ac}}{2a} = 3.70115(55) \times 10^{-4} \text{ and } -4.3027973(10). \tag{24}$$

The second solution is unphysical because δ_n is defined to be positive and much smaller than 1. Therefore $\delta_n = 3.70115(55) \times 10^{-4}$. Note that δ_n is more than 180 times smaller than Q_{nex}. This tiny proportion indicates that the charge distribution shift provided by δ_n is very slight.

3.1.2. Charge Arcs as Quantum Networks

In the refined GSQV proton model developed in Reference [9], the fine-tuned adjustable parameter, $R = 0.76273$ fm, agrees with $\lambda_p/\sqrt{3} \approx 0.76292$ fm to 3-digit precision, where

$$\lambda_p = \frac{h}{m_p c} \tag{25}$$

is proton Compton wavelength. This paper models unbound GSQV nucleons as self-sustaining networks of one-dimensional harmonic waves in 3+1 spacetime dimensions. This involves assuming

$$R_p = \frac{\lambda_p}{\sqrt{3}} \text{ and } R_n = \frac{\lambda_n}{2}. \tag{26}$$

Section 3.1.3 proposes that radial ensembles of virtual photon standing waves generate the charge arcs. It will be assumed that the radial systems of virtual photon standing waves interfere with the virtual photon standing waves–assumed to exist between the equatorial points of the proton inner arcs and the polar points of the neutron inner arcs.

Suppose the GSQV proton has both fundamental and second harmonic equatorial standing waves between the equatorial points of its inner charge arcs–shown in Figure 2. Since these equatorial points are λ_p apart, the wavelength of the fundamental harmonic will be $2\lambda_p$ with momentum $h/2\lambda_p$. If the virtual standing waves generating the proton charge arcs are fundamental harmonics, they will be of wavelength $2\lambda_p/\sqrt{3}$ with momentum $\sqrt{3}h/2\lambda_p$. The rms value of the sum of interfering momenta $h/2\lambda_p$ and $\sqrt{3}h/2\lambda_p$ is given by

$$p_{\mathrm{rms}} = \frac{h}{2\lambda_p}\sqrt{1^2 + \left(\sqrt{3}\right)^2} = \frac{h}{\lambda_p}, \tag{27}$$

which is the momentum of the second harmonic presumed to exist between the equatorial points of the GSQV proton's inner charge arcs. This second-harmonic standing wave, with wavelength λ_p, was a key assumption used to develop the original GSQV proton model in Reference [9]. This paper therefore proposes that the ensemble of an unbound GSQV proton's charge arc fundamental harmonics interfere with its equatorial fundamental harmonic to generate the second equatorial harmonic–quantized as the rms value of this interference.

Similarly, suppose that the neutron has both fundamental and second harmonic standing waves between the polar points of its inner charge arcs–shown in Figure 4. Since these polar points are $\sqrt{3}\lambda_n/2$ apart, the wavelength of the fundamental harmonic will be $\sqrt{3}\lambda_n$. Such a wave has momentum $h/\sqrt{3}\lambda_n$. If the virtual standing waves generating the neutron charge arcs are fundamental harmonics, they will be of wavelength λ_n with momentum h/λ_n. The rms value of the sum of interfering momenta $h/\sqrt{3}\lambda_n$ and h/λ_n is given by

$$p_{\mathrm{rms}} = \frac{h}{\lambda_n}\sqrt{\left(\frac{1}{\sqrt{3}}\right)^2 + 1^2} = \frac{2h}{\sqrt{3}\,\lambda_n}, \tag{28}$$

which is the momentum of the second harmonic presumed to exist between the polar points of the GSQV neutron's inner charge arcs. This second-harmonic standing wave has wavelength $\sqrt{3}\lambda_n/2$, which is the polar-point separation shown in Figure 4. This paper therefore proposes that the ensemble of an unbound GSQV neutron's charge arc fundamental harmonics interfere with its polar fundamental harmonic to generate the second polar harmonic–quantized as the rms value of this interference.

3.1.3. Charge Arc Generation and Proton Charge-Exclusion Zone

This paper proposes that the charge structure of an unbound GSQV nucleon consists of a pair of positive charge arcs and a pair of negative charge arcs. These are shown in Figures 1 and 2 for the GSQV proton and Figures 3 and 4 for the GSQV neutron. The outermost point of each charge arc resides at the zitterbewegung equator. Each charge arc is proposed to toroidally revolve about the particle center with its outermost point moving at light speed. This charge motion is proposed to generate the nucleon magnetic moments.

A proton's $+e$ net charge, and positive magnetic moment, is proposed to be generated from a pair of negative charge arcs, each with charge $-e/2$, revolving inside a pair of positive charge arcs, each with charge $+e$. These charge arcs are depicted in Figures 1 and 2. A neutron's zero net charge, and negative magnetic moment, is proposed to consist of a pair of positive charge arcs, each with charge $+e$, revolving inside a pair of negative charge arcs, each with charge $-e$. These charge arcs are depicted in Figures 3 and 4.

An ensemble of virtual photon standing waves is proposed to connect each point on a charge arc to its radial center. Each radial center resides on the zitterbewegung equator–substantially closer to the nucleon center than the arc's equatorial point. Each radial center coherently revolves about the particle center with the charge arc.

For unbound GSQV nucleons, the zitterbewegung effect [8,9,37–39,73–81] will be assumed to behave as a circulation of nucleon mass energy. Since unbound low-energy nucleons are spin-half particles, two loops of circulation represent a full zitterbewegung cycle. This mass-energy flow will be modeled as a type of power that will be called zitterbewegung inertial power (ZIP). This ZIP power may be interpreted as the rate at which the mass-energy of an unbound GSQV nucleon progresses forward in time. This may align with energetic causal set theory–where spacetime emerges from

Preprints.org (www.preprints.org) | NOT PEER-REVIEWED | Posted: 14 May 2024 doi:10.20944/preprints202405.0932.v1

momentum space and the conservation of energy-momentum [14–21]. Unbound GSQV nucleon ZIP will be defined as

$$P_N = E_N f_N, \tag{29}$$

where $E_N = hf_N$ is nucleon mass energy, and Compton frequency, f_N, is the number of full zitterbewegung cycles per second. Therefore

$$P_N = hf_N^2. \tag{30}$$

It will be assumed that an ensemble of virtual photons forms an ensemble of one-dimensional standing waves between every point on a charge arc and its radial center. Each charge arc is therefore continually reflecting and accelerating an ensemble of virtual photons. Each charge arc is a poloidal structure with poloidal radius R_N, which takes the value $R_N = R_p = \lambda_p/\sqrt{3}$ for the proton or $R_N = R_n = \lambda_n/2$ for the neutron.

For each unbound GSQV nucleon, vacuum energy poloidal acceleration density per poloidal radian will be assumed to be divided evenly among four charge arcs:

$$\frac{da_{\text{pol}}}{d\phi} = \tfrac{1}{4} R_N \omega_N^2, \tag{31}$$

where a_{pol} denotes the magnitude of poloidal centripetal acceleration, ϕ denotes latitude, and Compton angular frequency, $\omega_N = 2\pi f_N$, implies the key assumption that unbound GSQV nucleon charge and mass regenerate at the same rate. This assumption is explored in Section 3.1.5.

Since R_N and ω_N are independent of ϕ, it is trivial to integrate Equation (31) to obtain the total poloidal acceleration for each charge arc:

$$a_{\text{pol}} = \tfrac{1}{4} R_N \omega_N^2 \int_{\text{arc}} d\phi = \tfrac{1}{4} R_N \omega_N^2 \Delta\phi_{\text{arc}} = \tfrac{1}{4} s \omega_N^2, \tag{32}$$

where $\Delta\phi_{\text{arc}}$ is the poloidal angular extent of the charge arc, and s is poloidal charge arc length. Compton angular frequency, ω_N, may be interpreted as the temporal rate at which charge, q_{arc}, is regenerated on arclength, s. This rate is tied to nucleon Compton or zitterbewegung frequency, $f_N = \omega_N/2\pi$, and is independent of arclength, s.

Note that magnetic moment is generated by toroidal charge circulation. Poloidal acceleration, a_{pol}, is due to the circular polarization of the revolving virtual photon assumed to initially generate the GSQV nucleon during pair production [9]. Therefore poloidal acceleration, a_{pol}, is a circulation of virtual fields. This virtual field circulation is assumed to generate the four charge arcs of an unbound GSQV nucleon. The classical Larmor formula [112] will be repurposed to describe the amount of ZIP, P_{pol}, that couples with the four poloidal virtual field accelerations to generate the four charge arcs:

$$P_{\text{pol}} = 4\frac{q_{\text{arc}}^2 a_{\text{pol}}^2}{6\pi\varepsilon_0 c^3}, \tag{33}$$

where ε_0 is the electric permittivity of free space. Note that the classical Larmor formula is closely associated with the quantum Unruh effect [62,113–118].

Following Reference [9], Q_{pex} is defined as the uncharged (polar) proportion of the GSQV proton's outer surface. This outer surface is a surface of revolution formed by the GSQV proton's outer charge arcs. It can be seen from Figure 6 that the uncharged proportion of the GSQV proton's outer surface should resemble a flat cap at each pole. The quantity $(1 - Q_{pex})$ represents the charged proportion of

Preprints.org (www.preprints.org) | NOT PEER-REVIEWED | Posted: 14 May 2024 doi:10.20944/preprints202405.0932.v1

the GSQV proton's outer surface. Since vacuum energy reflects only from the charged portion of each arc, it is reasonable to assume that for an unbound GSQV proton,

$$P_{\rm pol} = (1 - Q_{pex})P_p = (1 - Q_{pex})hf_p^2 \tag{34}$$

For each proton outer charge arc, $R_p = \lambda_p/\sqrt{3}$ and $\Delta\phi_{\rm arc} = \pi$. These quantities are depicted in Figure 1. Substituting into Equation (32) yields

$$a_{\rm pol} = \frac{\pi\lambda_p}{4\sqrt{3}}\omega_p^2. \tag{35}$$

The relation $E_N = hc/\lambda_N = \hbar\omega_N$ implies $\lambda_N\omega_N = 2\pi c$. Therefore

$$\lambda_N\omega_N^2 = 2\pi c\omega_N = 4\pi^2 c f_N, \tag{36}$$

since $\omega_N = 2\pi f_N$.

Substituting Equation (36) into Equation (35) yields

$$a_{\rm pol} = \frac{\pi^3}{\sqrt{3}}cf_p. \tag{37}$$

Squaring,

$$a_{\rm pol}^2 = \frac{\pi^6}{3}c^2 f_p^2. \tag{38}$$

Substituting Equation (38) into Equation (33), with $q_{\rm arc} = e$, yields

$$P_{\rm pol} = \frac{2\pi^5 e^2 f_p^2}{9\varepsilon_0 c}. \tag{39}$$

Substituting Equation (34) into Equation (39) yields

$$(1 - Q_{pex})h = \frac{2\pi^5 e^2}{9\varepsilon_0 c}. \tag{40}$$

Rearranging,

$$e^2 = \frac{9\varepsilon_0 hc}{2\pi^5}(1 - Q_{pex}). \tag{41}$$

At low energies, the fine-structure constant may now be written as

$$\alpha = \frac{e^2}{2\varepsilon_0 hc} = \frac{9}{4\pi^5}(1 - Q_{pex}). \tag{42}$$

Presuming Equation (42) to be exact, the 2018 CODATA value [35,36],

$$\alpha = 7.2973525693(11) \times 10^{-3}, \tag{43}$$

can be used to calculate

$$Q_{pex} = 1 - \tfrac{4}{9}\pi^5\alpha = 1 - \alpha\pi^5\left(\frac{q_u}{e}\right)^2 = 7.49620754(15) \times 10^{-3}. \tag{44}$$

This value is entirely reasonable, since it is just 2.1% larger than that estimated in Reference [9]. Also note that Q_{pex} is only 2.7% larger than α. Surprisingly, the low-energy fine-structure constant is

 doi:10.20944/preprints202405.0932.v1

found to depend only on the proportionate area of the GSQV proton's charge-exclusion zone in 3+1 spacetime dimensions. At low energies, additional hidden dimensions may not be required to explain the coupling constant, α, that enables the unrivaled precision of quantum electrodynamics [90–92].

Planck charge, q_P, may now be written in terms of quantized electronic charge, e, and the low-energy fine-structure constant, α, as

$$q_P^2 = \frac{e^2}{\alpha} = \frac{4\pi^5 e^2}{9(1 - Q_{\text{pex}})}, \tag{45}$$

where e^2 was divided by the right-hand expression in Equation (42). Taking the square root,

$$q_P = \frac{2e}{3}\sqrt{\frac{\pi^5}{(1 - Q_{\text{pex}})}} = q_u\sqrt{\pi^5/(1 - Q_{\text{pex}})}, \tag{46}$$

where $q_u = 2e/3$ is the charge of an up, charm, or top quark. Rearranging,

$$q_u = q_P\sqrt{(1 - Q_{\text{pex}})/\pi^5}, \tag{47}$$

Surprisingly up, charm, and top quark charge appears to depend only on Planck charge, the proportionate area of an unbound GSQV proton's charge-exclusion zone, and π. It follows that

$$q_d = \frac{q_P}{2}\sqrt{(1 - Q_{\text{pex}})/\pi^5}, \tag{48}$$

where $q_d = e/3$ is the charge of a down, strange, or bottom quark.

Since $Q_{\text{pex}} \approx \alpha$,

$$q_u \approx q_P\sqrt{(1 - \alpha)/\pi^5} \approx 0.056955\, q_P \;\text{ and }\; q_d \approx \frac{q_P}{2}\sqrt{(1 - \alpha)/\pi^5} \approx 0.028478\, q_P. \tag{49}$$

To the same level of precision, the actual relationships are

$$q_u = \frac{2}{3}\sqrt{\alpha}\, q_P \approx 0.056950\, q_P \;\text{ and }\; q_d = \frac{1}{3}\sqrt{\alpha}\, q_P \approx 0.028475\, q_P. \tag{50}$$

Therefore Equation (49), which eliminates the $2/3$ and $1/3$ factors, overestimates quark charges by only 1 part in 10,000. However, note that Eqns. (47) and (48) also eliminate the $2/3$ and $1/3$ factors and are presumed exact.

Substituting $Q_{pex} \approx \alpha$ into Equation (42) yields

$$\frac{1}{\alpha} \approx \frac{4\pi^5}{9} + 1 = \left(\tfrac{2}{3}\right)^2 \pi^5 + 1 = \left(\tfrac{q_u}{e}\right)^2 \pi^5 + 1 \approx 137.01, \tag{51}$$

which is accurate to 4 digits. Note that Equation (51) is much simpler, although less accurate, than Equation (59) of Reference [119]. The next section shows how the low-energy fine-structure constant can be calculated to 5-digit precision from the unbound nucleon charge arc quantum networks developed in this paper.

3.1.4. Five Digit Precision

Extending the assumption applied in Equation (34), mass energy coupling with each type of charge arc will be defined as

$$P_{\text{pol}} = \beta_{\text{arc}}(1 - Q_{\text{pex}})P_N = \beta_{\text{arc}}(1 - Q_{\text{pex}})hf_N^2, \tag{52}$$

 doi:10.20944/preprints202405.0932.v1

where $\beta_{\text{arc}} \leq 1$ depends on charge arc type. Note that each charge arc type exists as a pair, and that the same nucleon mass energy is assumed to simultaneously couple with all four charge arcs of an unbound GSQV nucleon.

Comparing Equation (34) to Equation (52), $\beta_{po} = 1$ for the proton outer charge arcs. For each proton inner charge arc, $R_p = \lambda_p/\sqrt{3}$ and $\Delta\phi_{\text{arc}} = 2\phi_{pl}$. These quantities are depicted in Figure 2. Substituting into Equation (32) and applying Equation (36) yields

$$a_{\text{pol}} = \frac{2\pi^2}{\sqrt{3}} c\phi_{pl} f_p. \tag{53}$$

Squaring,

$$a_{\text{pol}}^2 = \frac{4\pi^4}{3} c^2 \phi_{pl}^2 f_p^2. \tag{54}$$

Substituting Equation (54) into Equation (33), with $q_{\text{arc}} = e/2$, yields

$$P_{\text{pol}} = \frac{2\pi^3 \phi_{pl}^2 e^2 f_p^2}{9\varepsilon_0 c}. \tag{55}$$

Substituting Equation (52) into Equation (55) yields

$$\beta_{pi}(1 - Q_{\text{pex}})h = \frac{2\pi^3 \phi_{pl}^2 e^2}{9\varepsilon_0 c}. \tag{56}$$

Rearranging,

$$e^2 = \frac{9\beta_{pi}\varepsilon_0 hc}{2\pi^3 \phi_{pl}^2}(1 - Q_{\text{pex}}). \tag{57}$$

Comparing with Equation (41),

$$\beta_{pi} = \frac{\phi_{pl}^2}{\pi^2}. \tag{58}$$

For each neutron outer charge arc, $R_n = \lambda_n/2$ and $\Delta\phi_{\text{arc}} = \pi$. These quantities are depicted in Figure 3. The reason why the outer charge arcs, in both unbound GSQV nucleon models, should extend for π radians is as follows: Charge is assumed to be regenerated by twin poloidal revolutions phase-locked with each other. Another assumption, is that at each moment in time, at most one inner and one outer charge arc can be regenerated. Therefore, whenever both phase-locked poloidal circulations are on outer arcs, only one can regenerate charge.

Substituting into Equation (32) and applying Equation (36) yields

$$a_{\text{pol}} = \frac{\pi^3}{2} c f_n. \tag{59}$$

Squaring,

$$a_{\text{pol}}^2 = \frac{\pi^6}{4} c^2 f_n^2. \tag{60}$$

Substituting Equation (60) into Equation (33), with $q_{\text{arc}} = e$, yields

$$P_{\text{pol}} = \frac{\pi^5 e^2 f_n^2}{6\varepsilon_0 c}. \tag{61}$$

Preprints.org (www.preprints.org) | NOT PEER-REVIEWED | Posted: 14 May 2024 doi:10.20944/preprints202405.0932.v1

Substituting Equation (52) into Equation (61) yields

$$\beta_{no}(1 - Q_{\text{pex}})h = \frac{\pi^5 e^2}{6\varepsilon_0 c}. \tag{62}$$

Rearranging,

$$e^2 = \frac{6\beta_{no}\varepsilon_0 hc}{\pi^5}(1 - Q_{\text{pex}}). \tag{63}$$

Comparing with Equation (41),

$$\beta_{no} = \frac{3}{4}. \tag{64}$$

For each neutron inner charge arc, $R_n = \lambda_n/2$ and $\Delta\phi_{\text{arc}} = 2\pi/3$. These quantities are depicted in Figure 4. Substituting into Equation (32) and applying Equation (36) yields

$$a_{\text{pol}} = \frac{\pi^3}{3} c f_n. \tag{65}$$

Squaring,

$$a_{\text{pol}}^2 = \frac{\pi^6}{9} c^2 f_n^2. \tag{66}$$

Substituting Equation (66) into Equation (33), with $q_{\text{arc}} = e$, yields

$$P_{\text{pol}} = \frac{2\pi^5 e^2 f_n^2}{27\varepsilon_0 c}. \tag{67}$$

Substituting Equation (52) into Equation (67) yields

$$\beta_{ni}(1 - Q_{\text{pex}})h = \frac{2\pi^5 e^2}{27\varepsilon_0 c}. \tag{68}$$

Rearranging,

$$e^2 = \frac{27\beta_{ni}\varepsilon_0 hc}{2\pi^5}(1 - Q_{\text{pex}}). \tag{69}$$

Comparing with Equation (41),

$$\beta_{ni} = \frac{1}{3}. \tag{70}$$

Average neutron mass energy coupling with its charge arcs,

$$\overline{\beta_n} = \frac{(\beta_{no} + \beta_{ni})}{2}(1 - Q_{pex}) = \frac{\left(\frac{3}{4} + \frac{1}{3}\right)}{2}(1 - Q_{pex}) \approx 0.537606, \tag{71}$$

where the value of Q_{pex} is obtained from Equation (44). Average proton mass energy coupling with its charge arcs,

$$\overline{\beta_p} = \frac{(\beta_{po} + \beta_{pi})}{2}(1 - Q_{pex}) = \frac{(1 + \phi_{pl}^2/\pi^2)}{2}(1 - Q_{pex}) \approx 0.599996, \tag{72}$$

where $\phi_{pl} = \cos^{-1}(1 - \sqrt{3}/2)$. When rounded to 5 digits, $\overline{\beta_p}$ is the same as 3/5. The quantity Q_{pex} will now be recalculated from ϕ_{pl} and the assumption $\overline{\beta_p} = 3/5$:

$$\overline{\beta_p} = \frac{(1 + \phi_{pl}^2/\pi^2)}{2}(1 - Q_{pex}) = \frac{3}{5}. \tag{73}$$

Rearranging,

$$Q_{pex} = \frac{\phi_{pl}^2 - \pi^2/5}{\pi^2 + \phi_{pl}^2} \approx 7.4897836 \times 10^{-3}. \tag{74}$$

Substituting Equation (74) into Equation (42) yields

$$\frac{1}{\alpha} \approx \frac{10\pi^3}{27}\left(\pi^2 + \phi_{pl}^2\right) \approx 137.03511, \tag{75}$$

which implies

$$\alpha \approx 7.2973998 \times 10^{-3}. \tag{76}$$

This agrees to five-digit precision with the established experimental value 7.2973526×10^{-3} [35,36] rounded to the same level of precision. This is more than four times more accurate than

$$\alpha = \left(\tfrac{3}{32}\right)^2 \exp\left[\tfrac{2}{3}\left(\tfrac{1}{3} - \sqrt{\tfrac{3}{8}}\right)\right] \approx 7.2971363 \times 10^{-3}, \tag{77}$$

calculated from Equation (59) of Reference [119]. Note that the fine-structure constant is known to increase with energy, and that the value obtained from Equation (75) and shown in Equation (76) is slightly larger than the experimentally established ground-state value. This is not the case with Equation (77). Could Eqns. (73) to (76) correspond to an energy above which an unbound GSQV nucleon transforms into a minimally excited state, as depicted in Figure 7?

The up and down quark charges may be estimated by substituting Equation (74) into Equations (47) and (48):

$$q_u \approx q_P\sqrt{6/\left[5\pi^3\left(\pi^2 + \phi_{pl}^2\right)\right]} \approx 1.068121 \times 10^{-19}\ \mathrm{C} \tag{78}$$

and

$$q_d \approx q_P\sqrt{3/\left[10\pi^3\left(\pi^2 + \phi_{pl}^2\right)\right]} \approx 5.340606 \times 10^{-20}\ \mathrm{C}, \tag{79}$$

which are accurate to at least 5 digits compared to the exact SI base unit values,

$$q_u = \frac{2e}{3} = 1.068117756 \times 10^{-19}\ \mathrm{C} \ \text{ and } \ q_d = \frac{e}{3} = 5.34058878 \times 10^{-20}\ \mathrm{C}, \tag{80}$$

defined in 2019 [35,36]. Note that Equations (47) and (48) are simpler than Equations (78) and (79) and are presumed exact.

3.1.5. Nucleon Charge and Mass Coupling

For most of the known unstable particles, decay times are well established [5]. However, very little is known about particle formation times [120]. It is plausible that a nucleon's charge and mass

Preprints.org (www.preprints.org) | NOT PEER-REVIEWED | Posted: 14 May 2024 doi:10.20944/preprints202405.0932.v1

creation, annihilation, and regeneration all occur on the timescale equal to the length of the nucleon's zitterbewegung cycle. This is the time, t_z, for light to travel a nucleon Compton wavelength, λ_N:

$$t_z = \frac{\lambda_N}{c} \approx 4.4 \times 10^{-24}\ \text{s}, \tag{81}$$

which is the same order of magnitude as the strong interaction timescale. This may conceptually align with energetic causal set theory–where stable particles may continually regenerate themselves at each moment in time [14–21].

Substituting Equation (42) into Equation (52) yields

$$P_{\text{pol}} = \frac{4\pi^5}{9}\beta_{\text{arc}}\,\alpha P_N = k_{\text{arc}}P_N, \tag{82}$$

where

$$k_{\text{arc}} = \frac{4\pi^5}{9}\beta_{\text{arc}}\,\alpha \tag{83}$$

represents the coupling between nucleon mass and each type of charge arc. Section 3.1.4 derived the β_{arc} values: $\beta_{po} = 1$; $\beta_{pi} = \phi_{pl}^2/\pi^2$; $\beta_{no} = 3/4$; and $\beta_{ni} = 1/3$. Substituting these values into Equation (83), using the 2018 CODATA value, $\alpha = 7.2973525693(11) \times 10^{-3}$ [35,36], and $\phi_{pl} = \cos^{-1}(1 - \sqrt{3}/2)$ yields the nucleon mass-to-charge coupling constants:

$$k_{po} = \frac{4\pi^5}{9}\alpha = 0.99250379246(15); \tag{84}$$

$$k_{pi} = \frac{4\pi^3}{9}\phi_{pl}^2\,\alpha = 0.20748840645(31); \tag{85}$$

$$k_{no} = \frac{\pi^5}{3}\alpha = 0.74437784434(11); \tag{86}$$

and

$$k_{ni} = \frac{4\pi^5}{27}\alpha = 0.330834597485(50). \tag{87}$$

It is apparent from Equations (71) and (72) that an unbound GSQV neutron's mass energy couples with its charge arcs only about 10% less than an unbound GSQV proton's mass energy couples with its charge arcs. However, Equations (84) to (87) show that nucleon mass energy couples much more with outer charge arcs than inner charge arcs, and that this coupling ratio is more than twice as much for the unbound GSQV proton as it is for the unbound GSQV neutron:

$$\frac{k_{po}}{k_{pi}} > 2\,\frac{k_{no}}{k_{ni}}. \tag{88}$$

Also note that

$$\frac{1 - k_{no}}{1 - k_{po}} \approx 34, \tag{89}$$

which implies that GSQV neutron outer charge arcs are about 34 times less coupled with mass energy compared to GSQV proton outer charge arcs.

Preprints.org (www.preprints.org) | NOT PEER-REVIEWED | Posted: 14 May 2024 doi:10.20944/preprints202405.0932.v1

3.2. Quarks and Neutron Decay

3.2.1. Quark Formation

When minimally excited above its ground state, about 1-2% of an unbound GSQV nucleon's mass energy may couple with the Higgs field and transfer from the GSQV nucleon's central zitterbewegung fermion to its system of revolving formerly-massless charge arcs. As proposed in Reference [9], for the proton, this process may initially form three valence quarks and a virtual $u\bar{u}$ quark pair that initializes the formation of a virtual pion cloud.

A neutral pion exists as the slightly imbalanced superposition of bound $u\bar{u}$ and $d\bar{d}$ quark pairs [110]. The imbalance is due to unequal bare quark masses. Since bare down quarks are more massive than bare up quarks [5], it will be assumed that the GSQV proton's precursor, to a virtual neutral pion, is purely the lower energy $u\bar{u}$ quark pair. Note that this paper assumes that the virtual $u\bar{u}$ quark pairs shown in Figure 7 are initially unbound sea quarks.

3.2.2. Intrinsic Charm Quark Formation

In addition to a minimally excited unbound GSQV proton containing an initial unbound $u\bar{u}$ virtual quark pair, which may bind and initialize a virtual neutral pion, the same unbound $u\bar{u}$ virtual quark pair may occasionally transform into a charm quark, c, and an anticharm quark, $\bar{c}$. This unbound $c\bar{c}$ quark pair may momentarily bind with the proton's three valence quarks to form bound states such as $|uudc\bar{c}\rangle$ [1,40–50]. The instrinsic charge values do not change, since up and charm quarks are like-charged. However, a substantial amount of mass energy will need to be temporarily borrowed from, and returned to, the local vacuum. Therefore, a minimally excited unbound GSQV proton model may partly explain the experimental evidence for the proton's probabilistically small intrinsic $c\bar{c}$ component [1,40–50].

The unbound GSQV proton model may explain charm quark mass as follows: With both unbound GSQV nucleon models, charge is assumed to be regenerated by twin poloidal revolutions phase-locked with each other. Another assumption, is that at each moment in time, at most one inner and one outer charge arc can be regenerated. Therefore, whenever both phase-locked poloidal circulations are on an outer arc, only one can regenerate charge. This explains how the polar charge-exclusion zones form. With the unbound GSQV proton model, the uncharged polar poloidal circulation is divided into two paths as shown in Figure 6.

For the unbound GSQV neutron model, this phase locking prevents the twin poloidal vectors from overlapping. However, for the unbound GSQV proton model, the two poloidal vectors will occasionally overlap. As illustrated in Figure 2, two overlaps will occur almost simultaneously–half a poloidal cycle apart. Suppose each of these twin overlapping lengths momentarily forms a fundamental harmonic standing wave of vacuum energy. Each of these standing waves will be of wavelength

$$2\left(\frac{\lambda_p}{\sqrt{3}} - 2r_{pa}\right) = 2\lambda_p\left(1 - \frac{1}{\sqrt{3}}\right), \tag{90}$$

which is proportionately shorter than the wavelength of the fundamental harmonic ensemble regenerating the charge arcs, $2R_p = 2\lambda_p/\sqrt{3}$, by the factor

$$\sqrt{3} - 1. \tag{91}$$

The unbound GSQV proton's virtual optimal Möbius band relationship between charge and mass generation is assumed to hold. This momentary shortening of the R_p vector will be assumed

Preprints.org (www.preprints.org) | NOT PEER-REVIEWED | Posted: 14 May 2024 doi:10.20944/preprints202405.0932.v1

additive and equivalent to proton mass energy, $m_p \approx 938.272$ MeV/c^2 [5,35,36], increasing by the factor $(\sqrt{3}-1)^{-1}$. This will appear as a momentary increase in proton mass energy by the amount

$$\frac{m_p}{\sqrt{3}-1} \approx 1281.70 \text{ MeV/c}^2. \tag{92}$$

Since there are two momentary overlaps, the proton mass increase should appear to be twice this amount. This is more than enough mass energy to generate the charm and anticharm quark "running" masses [5].

Since the charge associated with this momentary increase in proton mass energy already exists in the form of a virtual unbound $u\bar{u}$ quark pair, the bare mass of an up quark [5] will be subtracted. Up quark bare mass at the charm quark "running" mass renormalization scale will be applied [5]. At the energy of the charm quark "running" mass, the up quark mass is close to 25% larger than that at 2.0 GeV [5]. In Section 3.3, Equation (103) estimates up quark mass as $m_u = 2.30^{+0.23}_{-0.10}$ MeV/c^2 on the 2.0 GeV scale. This becomes $m_u = 2.88^{+0.29}_{-0.13}$ MeV/c^2 when increased by 25%. We therefore estimate the mass energy of each intrinsic charm or anticharm quark as

$$m_c = \frac{m_p}{\sqrt{3}-1} - 2.88^{+0.29}_{-0.13} \text{ MeV/c}^2 = 1278.82^{+0.13}_{-0.29} \text{ MeV/c}^2. \tag{93}$$

Both Equation (92) and Equation (93) are well within the 2022 recommended Particle Data Group range: $m_c = 1270 \pm 20$ MeV/c^2 [5].

The twin charge-regenerating vectors are poloidally phase locked. However, they are generally in different planes which rotate toroidally with the charge arcs. This is because the equators of the inner and outer charge arcs rotate toroidally at the same speed (light speed), which implies a different toroidal frequency for each charge arc type. As shown in Figure 2, the twin charge-regenerating vectors align perfectly only on the zitterbewegung equator.

Suppose the twin charge-regenerating vectors become entangled whenever both vector tips, which is where charge is regenerated, are no farther from the zitterbewegung equator than the zitterbewegung radius, r_{cz} [9], of the charm quark "running" mass, m_c [5]. Also suppose that charm quark mass-energy is generated during such entanglement. During this charm quark mass-energy generation, the maximum angular separation, θ_{ent}, between each R_p vector and the zitterbewegung equator will be

$$\theta_{\text{ent}} = \sin^{-1}\left(\frac{r_{cz}}{R_p}\right) = \sin^{-1}\left(\frac{\sqrt{3}\,m_p}{4\pi m_c}\right). \tag{94}$$

It will be assumed that this angular separation will uniformly manifest as any combination of poloidal and toroidal misalignments. It is well known that such a uniform angular distribution will cover angular area $2\pi(1-\cos\theta_{\text{ent}})$. Since there are 4π steradians in a sphere, this angular area is

$$\frac{(1-\cos\theta_{\text{ent}})}{2} = \frac{1}{2}\left(1-\sqrt{1-\frac{3m_p^2}{16\pi^2 m_c^2}}\right) \approx 0.26\% \tag{95}$$

of the total spherical angular area, where the identity $\cos(\sin^{-1}(x)) = \sqrt{1-x^2}$ has been applied. This suggests that the $|uudc\bar{c}\rangle$ bound state occurs about 0.26% of the time. Since this momentary state includes two charm quark masses, and each charm quark "running" mass [5] is significantly larger than the proton mass, we estimate the fraction of the proton momentum carried by intrinsic charm quarks as

$$\frac{m_c}{m_p}(1-\cos\theta_{\text{ent}}) = \frac{m_c}{m_p} - \sqrt{\left(\frac{m_c}{m_p}\right)^2 - \frac{3}{16\pi^2}} = 0.704(11)\%, \tag{96}$$

Preprints.org (www.preprints.org) | NOT PEER-REVIEWED | Posted: 14 May 2024 doi:10.20944/preprints202405.0932.v1

where the uncertainty is propagated from the 2022 recommended Particle Data Group range: $m_c = 1270 \pm 20$ MeV$/c^2$ [5]. Our estimate is consistent with the value $(0.62 \pm 0.28)\%$, reported in Reference [1], and at least an order of magnitude more precise. Note that all quantities calculated from proton mass, m_p, are time-averaged. The momentary intrinsic charm and anticharm quarks are assumed to exchange energy and momentum with the time-averaged proton energy and momentum. The Heisenberg uncertainty principle allows intrinsic fluctuations of proton energy and momentum on short timescales [121,122].

3.2.3. Gluon Flux Tube Formation

Except for the unbound GSQV neutron's outer charge arc pair, all other unbound nucleon charge arc pairs must merge before decomposing into the quark charge values shown in Figure 7. Such merging presumably momentarily forms charge shells [9]. It can be seen from the right-hand column of Panel (a) of Figure 7 that the two neutron outer charge arcs do not necessarily need to merge before decomposing into the four quarks shown. It is important to remember that color charge cycles extremely rapidly–to the degree that the color charge of each valence quark is effectively the superposition of all three colors and the color charge of each sea quark is the superposition of all three colors and all three anticolors.

The remaining 98-99% of a minimally excited unbound GSQV nucleon's mass energy is proposed to transform into gluon flux tubes and quark relativistic kinetic energy [123]. This paper proposes that the curvature of the unbound GSQV charge arcs and charge shells prevents the initial formation of gluon flux tubes between quarks on the same arc or shell. It will therefore be assumed that initially two gluon flux tubes form between inner and outer valence quarks. In particular, each of two outer valence quarks connects to the same inner valence quark via a gluon flux tube. It will be assumed that this initial double gluon flux tube structure immediately transforms into the three-way symmetric gluon flux tube structure described by the Standard Model of particle physics [123].

The nucleon's spin angular momentum may partially migrate from the gluon flux tubes to the valence quarks [9]. This partial migration may be interaction-dependent and provide a conceptual clue to the nucleon spin crisis [9,124–126].

For the minimally excited unbound GSQV proton, Panel (b) of Figure 7 illustrates the transition from massless charge arcs to massive quarks. The proton's two up valence quarks originate from its outer charge arcs, while the proton's down valence quark originates from its inner charge arcs. Comparing Figures 1 and 2, clearly the proton's inner arcs are less symmetrical than its outer arcs. Therefore, the proton's up-quark probability distribution should be more symmetrical than its down-quark probability distribution. This expected effect has been confirmed to occur in recent lattice QCD computations [34].

For the minimally excited unbound GSQV neutron, Panel (a) of Figure 7 illustrates the transition from massless charge arcs to massive quarks. The neutron's two down valence quarks originate from its outer charge arcs, while the neutron's up valence quark originates from its inner charge arcs. The minimally excited unbound GSQV neutron contains two unbound $u\bar{u}$ quark pairs that are proposed to initialize the formation of a virtual pion cloud.

3.2.4. Neutron Decay

The long-established neutron decay mechanism is for a down valence quark to decay to an up valence quark via the emission of a W^- boson or absorption of a W^+ boson [127]. Both processes are equivalent and emit an electron and an electron antineutrino. The unbound GSQV nucleon models offer the following similar, but more detailed, mechanism. Suppose that the weak interaction [110] involves one of the unbound GSQV neutron's outer charge arcs either transforming into a W^- boson or absorbing a W^+ boson. Note that in the minimally excited GSQV neutron model, illustrated in Panel (a) of Figure 7, each outer charge arc initially transforms into an unbound $\bar{u}d$ quark pair. The Standard Model allows a W boson to both form from, and decay into, a first-generation quark pair

 doi:10.20944/preprints202405.0932.v1

[123]. Examples include leptonic decay of a charged pion and charged kaon decay into three charged pions. It is therefore plausible that the weak interaction [110] applies to the absolute ground state of the GSQV neutron model as well as its minimally excited state illustrated in Panel (a) of Figure 7.

Panel (b) of Figure 7 shows that the minimally excited unbound GSQV proton model does not contain an intrinsic $\bar{\mathrm{d}}$ quark (charge $+e/3$). The absence of an intrinsic $\bar{\mathrm{d}}$ sea quark may be associated with proton stability. An $\bar{\mathrm{d}}$ quark would presumably be needed to either form and emit a W^+ boson from an $\mathrm{u}\bar{\mathrm{d}}$ quark pair, or annihilate with an $\bar{\mathrm{u}}\mathrm{d}$ quark pair that decomposes from an absorbed W^- boson. Note that the electron capture [107–110] and positron emission [128] processes may generally involve a W boson interacting with a loosely bound proton's inner charge region, which is more likely to occur with the assistance of other bound nucleons [111]. Section 3.1.1 discusses some details of how this paper's GSQV nucleon models explain aspects of electron capture.

Once an unbound GSQV neutron has emitted a W^- boson, or absorbed a W^+ boson, it will resemble an inside-out unbound GSQV proton. Such an inside-out configuration should be electromagnetically unstable. All other parameters remaining unchanged, Equation (18) will now be modified by removing $-e$ from the neutron's outer charge arcs. This halves the charge on the outer arcs, so that the former neutron's magnetic moment becomes

$$\mu = \left(\frac{V_{ni}}{(1+\delta_n)} - \frac{V_{no}}{18(1-\delta_n)(1-Q_{\mathrm{nex}})} \right) \frac{8}{\pi\lambda_n^2 r_{pz}} \mu_N \approx +0.623\, \mu_N, \tag{97}$$

which is of opposite magnetic polarity to the neutron. This magnetic moment is also considerably weaker than that of either free nucleon.

Suppose that electrostatic effects dominate the dynamics of this magnetically weakened environment. The former neutron's inner charge region will have a far greater charge density than its outer charge region. It will be assumed that this causes the inner positive charge region to expand outward, which should result in an increasingly positive magnetic moment. This outward expansion could conceivably stop once the perturbed nucleon's magnetic moment becomes strong enough to contain the charge structures via the unbound GSQV nucleon's magnetic self-interaction. Details of such self-interaction are subjectively described in Reference [9]. It will be assumed that the expansion of the inner positive charge region will not stop until after it has completely passed through the negative charge region. This new structure is assumed to stabilize once it becomes identical to that of an unbound GSQV proton–with its twin virtual optimal Möbius bands [10–13]. See Section 3.1 and Appendix A for details.

For the decay process of a minimally excited GSQV neutron, it will be assumed that a similar electromagnetic restructuring occurs. In addition, the trilateral gluon flux tube structure must disconnect from the down valence quark that combines with an intrinsic antiup sea quark. This unbound $\bar{\mathrm{u}}\mathrm{d}$ quark pair will presumably either form and emit a W^- boson or annihilate with a $\mathrm{u}\bar{\mathrm{d}}$ quark pair that decomposes from an absorbed W^+ boson. The trilateral gluon flux tube structure then presumably connects with an intrinsic up sea quark, causing it to transform into a valence up quark.

The Standard Model assumes that a valence quark may change flavor by emitting or absorbing a W^+ or W^- boson. Other quarks are not directly involved. The W^+ and W^- bosons share the same mass, m_{W}, which may be calculated from other Standard Model parameters. Reference [129] recently calculated the following Standard Model prediction of the W boson mass:

$$m_{\mathrm{W}} = 80354.5 \pm 5.9\ \mathrm{MeV/c^2}, \tag{98}$$

which is statistically consistent with the ATLAS Collaboration's recent experimental determination [130],

$$m_{\mathrm{W}} = 80366.5 \pm 9.8\ (\mathrm{stat.}) \pm 12.5\ (\mathrm{syst.}) = 80366.5 \pm 15.9\ \mathrm{MeV/c^2}. \tag{99}$$

Note that Reference [129] performs a global fit of electroweak data within the Standard Model without directly incorporating the first-generation quark masses.

This paper proposes the following unbound neutron decay process as an extension of the Standard Model:

1. An outer charge arc decomposes into an intrinsic unbound $\bar{u}d$ quark pair. This quark pair either forms and emits a W^- boson or annihilates with a $u\bar{d}$ quark pair that decomposes from an absorbed W^+ boson. This causes the decaying nucleon to initially lose mass equal to the sum of the bare masses of these intrinsic $\bar{u}$ and d quarks. This results in an unstable structure that is less massive than, but of the same charge as, a proton;
2. The inner charge arcs expand to become outer charge arcs and two new inner charge arcs form;
3. All four charge arc radii increase to the Compton wavelength of this restabilizing nucleon's mass divided by $\sqrt{3}$, which forms twin virtual optimal Möbius bands [10–13];
4. Once this virtual optimal Möbius band structure has formed, the restabilizing nucleon is assumed to have the same angular charge distribution and equatorial speed as that of an unbound GSQV proton;
5. Being less massive than a proton, this restabilizing nucleon will be larger than a proton. It will therefore have a lower charge density and larger magnetic moment compared to an unbound GSQV proton. Applying classical electromagnetism to this quantum system, the lower charge density is assumed to be associated with a lower tendency for outward expansion due to electrostatic forces. The larger magnetic moment is assumed to result in larger inward equatorial magnetic forces compared to an unbound GSQV proton [9];
6. This larger inward equatorial compression, combined with reduced outward expansion, is assumed to cause the restabilizing nucleon to uniformly contract–and thereby increase its mass–to that of an unbound proton. An unbound GSQV proton is assumed to be a balanced system of internal quantum electromagnetic interactions [9].

3.2.5. W Boson Mass

Note that this paper does not attempt to explain the absolute or relative values of the nucleon masses. This paper proposes that the W boson of the Standard Model should be amended by adding an up quark mass and a down quark mass. During leptonic decay of a charged pion [131], it is plausible that the W boson mass actually includes the bare masses of the pion's two quarks: one up or antiup; one down or antidown. For most W boson interactions, the principle applied by this paper is that quark flavor change necessarily involves up and down sea quarks. This implies that a second or third generation quark transforms into a first generation quark before emitting or absorbing a W boson. The converse also applies and each generation change will involve an exchange of mass and vacuum energies.

This paper assumes that the intrinsic properties of unbound nucleons are determined at the energy scale of nucleon-antinucleon pair production, which is about 2 GeV. At this energy scale, the sum of the up and down bare quark masses is approximately 6.9 MeV/c^2 [5], with a much smaller absolute uncertainty than of the W boson mass estimates in Equations (98) and (99). This paper therefore proposes amending Equation (98) by adding 6.9 MeV/c^2:

$$m_W = 80361.4 \pm 5.9 \text{ MeV/c}^2. \quad (100)$$

Note that the means of Equations (99) and (100) differ by only 5.1 MeV/c^2, which is less than both the statistical uncertainty of Equation (99) and the uncertainty of Equation (100). Clearly the neutron decay model proposed by this paper agrees substantially better with the recent analysis of the ATLAS Collaboration [130] than does the Standard model. The ATLAS Collaboration is expected to produce future W boson mass estimates with substantially lower uncertainty. It is possible that these future estimates could agree substantially more with the Standard Model than the model proposed by this paper. Such an outcome could falsify key aspects of the modeling proposed by this paper.

Preprints.org (www.preprints.org) | NOT PEER-REVIEWED | Posted: 14 May 2024 doi:10.20944/preprints202405.0932.v1

3.3. Improved Unbound GSQV Proton Model

The accuracy of this both this section and Section 3.4 depends on the precise sum of the up and down quark masses at the energy scale of nucleon-antinucleon pair production. This energy scale is approximately 2 GeV. At the 2 GeV energy scale, the sum of the up and down quark masses is experimentally determined to be [5]

$$m_u + m_d = 2\overline{m} = 6.90^{+0.70}_{-0.30}\ \mathrm{MeV/c^2}. \tag{101}$$

While this central estimate and uncertainties are appropriate for Equation (100) in Section 3.2.5, these uncertainties are much too large to convincingly demonstrate the claimed precision of the proton model developed in this section and the neutron model developed in Section 3.4.

Similarly, the experimentally determined up-to-down quark mass ratio [5],

$$\frac{m_u}{m_d} = 0.474^{+0.056}_{-0.074}\ \mathrm{MeV/c^2}, \tag{102}$$

is much too inaccurate for our purposes. Instead, this paper will assume the exact relationship $m_u = m_d/2$, which is well within the uncertainty of Equation (102). Combining this assumption with Equation (101) yields

$$m_d = \frac{4\overline{m}}{3} = 4.60^{+0.47}_{-0.20}\ \mathrm{MeV/c^2} \quad \text{and} \quad m_u = \frac{2\overline{m}}{3} = 2.30^{+0.23}_{-0.10}\ \mathrm{MeV/c^2}. \tag{103}$$

3.3.1. Theoretical Down Quark Mass

It is often speculated that the down quark mass, at the precise energy threshold of nucleon-antinucleon pair production, may be precisely 9 electron masses [5]:

$$m_d = 9m_e = 9 \times 0.51099895000(15)\ \mathrm{MeV/c^2} = 4.5989905500(14)\ \mathrm{MeV/c^2}, \tag{104}$$

which closely agrees with the central estimate in Equation (103).

This paper will apply this hypothesis and also propose that the down quark mass, at the precise energy threshold of nucleon-antinucleon pair production, is precisely the difference between the charged and uncharged pion masses [5,132]:

$$m_d = m_{\pi^\pm} - m_{\pi^0} = 4.59364(48)\ \mathrm{MeV/c^2}. \tag{105}$$

Note that Equations (104) and (105) differ by more than 11 standard deviations, and so are unlikely to be consistent with each other. At the precise energy threshold of nucleon-antinucleon pair production, suppose that virtual neutral pions are in equilibrium with virtual photons. Also suppose that the formation of a virtual charged pion pair requires the temporary borrowing of vacuum energy equal to the mass energy of an unbound bare $\mathrm{d\bar{d}}$ quark pair. A pair of virtual charged pions will then be formed from the d quark (charge $-e/3$) binding with an intrinsic $\bar{\mathrm{u}}$ quark and the $\bar{\mathrm{d}}$ quark (charge $+e/3$) binding with an intrinsic u quark. If this occurs, it is plausible that

$$m_{\pi^0} + m_d = m_{\pi^\pm}, \tag{106}$$

from which Equation (105) follows. Note the complete absence of antidown quarks (charge $+e/3$) and absence of sea down quarks (charge $-e/3$) in Figure 7, where no pions are present. Pions are assumed to form at higher energies.

In the minimally excited GSQV nucleon models, depicted in Figure 7, it is possible–but not necessary–that each unbound up and antiup quark possesses relativistic energy equaling the mass energy of a neutral pion. This may explain how these quarks are able to initiate charged pion

Preprints.org (www.preprints.org) | NOT PEER-REVIEWED | Posted: 14 May 2024 doi:10.20944/preprints202405.0932.v1

production. Reference [106] found that non-single-pion photoproduction off the proton amounts to about 10%, whereas non-single-pion photoproduction off the neutron amounts to about 44%. This large difference may be partly explained by the minimally excited GSQV neutron containing twice as many charged pion-production sites, in the form of virtual up and antiup sea quarks, as the minimally excited GSQV proton.

3.3.2. Perturbed Charge Distributions

Section 3.1.1 defined and calculated a parameter, δ_n, which represents a slight perturbation of the unbound GSQV neutron's charge distribution along each charge arc. This perturbation will be assumed due to the interaction between the radial vacuum standing wave ensemble, maintaining each charge arc, and the charge arc itself.

During Steps 3 & 4 of the unbound neutron decay process described in Section 3.2.4, new charge arcs form with radius, $R_{n'}$, equal to the Compton wavelength of the decaying neutron's temporarily reduced mass divided by $\sqrt{3}$. It will be assumed, that during Steps 3 & 4, the charge perturbation parameter changes with the inverse square of the charge arc radius. The reason for this inverse square relationship is as follows. The wavelength of the radial standing wave ensembles will increase linearly with charge arc radius, which will cause their energies to decrease linearly with arc radius. In addition, the energy density of these radial standing wave ensembles, along each charge arc, will dilute linearly with charge arc radius. The charge perturbation parameter is assumed proportional to this energy density, which declines with the square of charge arc radius.

It will be assumed that the charge perturbation parameter, $\delta_{n'}$, does not change further during Steps 5 & 6. Therefore define unbound proton charge perturbation parameter,

$$\delta_p = \delta_{n'} = \left(\frac{R_n}{R_{n'}}\right)^2 \delta_n = \left(\frac{\sqrt{3}m_{n'}}{2m_n}\right)^2 \delta_n = \frac{3}{4}\left(\frac{m_n - \frac{3}{2}m_d}{m_n}\right)^2 \delta_n, \tag{107}$$

since Compton wavelength is inversely proportional to mass and this paper assumes $m_u + m_d = \frac{3}{2}m_d$.

3.3.3. Cosmic Origin of Quark Masses

Reference [9] combines the zitterbewegung and circular Unruh effects to propose that proton mass energy is quantized as approximately $2\sqrt{3}/0.2855 \approx 98.9\%$ of the median thermal excess vacuum energy due to the circular Unruh effect. The approximate value 0.2855 is obtained by numerically integrating the Planck spectrum and the relationship $k_B T/0.2855 \approx 3.503 k_B T$, where k_B is the Boltzmann constant and T is temperature. A more precise numerical integration yields median thermal energy to be approximately $3.50302 k_B T$ [133]. Reference [133] argues that the median energy is the most physically meaningful numerical criterion for the thermal spectrum peak, and that this should be more widely taught.

In the early universe, unbound nucleons initially formed during the hadron epoch. Early in the hadron epoch, each unbound nucleon was completely surrounded by the quark-gluon plasma (QGP) from which it formed [134]. Prior to neutrino decoupling, protons were in equilibrium with neutrons and antiprotons were in equilibrium with antineutrons [134].

This paper proposes that each proton-neutron pair, and each antiproton-antineutron pair, of quantum vortices generated more than enough circular Unruh energy for the mass energy of each nucleon. It is proposed that these quantum vortices generated additional circular Unruh energy amounting to the bare mass energies of the nucleon pair's six valence quarks. This excess energy is proposed to replace the mass energies of the QGP quarks from which the nucleon pair formed. It is therefore proposed that

$$3.50302 k_B \left(T_p + T_n\right) \approx \left(m_p + m_n + 3m_u + 3m_d\right) c^2, \tag{108}$$

Preprints.org (www.preprints.org) | NOT PEER-REVIEWED | Posted: 14 May 2024 doi:10.20944/preprints202405.0932.v1

where T_p and T_n respectively represent the circular Unruh temperatures of the proton and neutron. Reference [9] shows that $T_p = \frac{m_p c^2}{2\sqrt{3}k_B}$, which implies $T_n = \frac{m_n c^2}{2\sqrt{3}k_B}$. Substuting into Equation (108) yields

$$\frac{3.50302}{2\sqrt{3}}\left(m_p + m_n\right) \approx m_p + m_n + 3m_u + 3m_d. \tag{109}$$

Rearranging and substituting proton and neutron mass values in units of MeV/c^2 [5,35,36] yields

$$m_u + m_d \approx \frac{1}{3}\left(\frac{3.50302}{2\sqrt{3}} - 1\right)\left(m_p + m_n\right) \approx 7.032 \text{ MeV/c}^2, \tag{110}$$

which is less than 2% above the central estimate in Equation (101). Since this paper assumes $m_u = m_d/2$,

$$m_d \approx \frac{2}{9}\left(\frac{3.50302}{2\sqrt{3}} - 1\right)\left(m_p + m_n\right) \approx 4.6882 \text{ MeV/c}^2, \tag{111}$$

which is only about 2% above the m_d values calculated from Eqns. (103), (104), and (105). The consistency between Eqns. (103), (104), (105), and (111) is encouraging. The additional 2% calculated by Equations (110) and (111) may be due to an intrinsic heavy quark component [1,40–50].

3.3.4. Proton Magnetic Moment from a Charge Arc Geometry

Following Reference [9], Section 3.1.1, and Section 3.3.2, proton magnetic moment will be calculated from

$$\mu_p = \left(\frac{2V_{po}}{(1+\delta_p)(1-Q_{\text{pex}})(R_p + r_{pa})^2} - \frac{V_{pi}}{(1-\delta_p)(R_p - r_{pa})^2}\right)\frac{\mu_N}{4\pi r_{pz}}, \tag{112}$$

where V_{pi} is the lemon volume formed by rotating the proton's two inner charge arcs about the proton center, V_{po} is the volume formed by rotating the proton's two outer charge arcs, with flat end caps, about the proton center, Q_{pex} is the uncharged proportion of the proton's outer surface, $R_p = \lambda_p/\sqrt{3}$, and

$$r_{pa} = R_p - \frac{\lambda_p}{2} = \lambda_p\left(\frac{1}{\sqrt{3}} - \frac{1}{2}\right). \tag{113}$$

Substituting Equations (1) and (113) into Equation (112) yields

$$\mu_p = \left(\frac{6V_{po}}{(1+\delta_p)(1-Q_{\text{pex}})(4-\sqrt{3})^2} - \frac{V_{pi}}{1-\delta_p}\right)\frac{4\,\mu_N}{\lambda_p^3}. \tag{114}$$

Following the Appendix of Reference [9],

$$V_{pi} = \frac{4}{3}\pi R_p^3\left[\sin^3\phi_{pl} - \frac{3}{4}\cos\phi_{pl}(2\phi_{pl} - \sin 2\phi_{pl})\right] \tag{115}$$

and

$$V_{po} = \pi^2 R_p^2\left(r_{pa} + \frac{4R_p}{3\pi}\right) + 2\pi r_{pa}^2 R_p. \tag{116}$$

Note that

$$\phi_{pl} = \cos^{-1}\left(\frac{r_{pa}}{R_p}\right) = \cos^{-1}\left(1 - \frac{\sqrt{3}}{2}\right). \tag{117}$$

Clearly, both V_{pi} and V_{po} are proportional to λ_p^3. The form of Equation (114) therefore implies a proton g-factor independent of proton mass.

Preprints.org (www.preprints.org) | NOT PEER-REVIEWED | Posted: 14 May 2024 doi:10.20944/preprints202405.0932.v1

The quantity Q_{pex} will be calculated from Equation (44); the quantity δ_p will be calculated from Equation (107). The uncertainty of δ_n, obtained from Equation (24), dominates the uncertainty of Equation (107) to the degree where the discrepancy between Equations (104) and (105) becomes negligible. Therefore, applying either Equation (104) or Equation (105) to Equation (107) yields

$$\delta_p = 2.7353(4) \times 10^{-4}. \tag{118}$$

Substituting Equation (118) into Equation (114) yields

$$\mu_p = 2.7928474(3)\ \mu_N, \tag{119}$$

which is consistent with experiment. However, proton magnetic moment has been experimentally determined to far greater precision [35,36,135]:

$$\mu_p = 2.79284734463(82)\ \mu_N. \tag{120}$$

It is clear from Equation (20) that δ_n depends on neutron mass, m_n, proton mass, m_p, and neutron magnetic moment, μ_n, which is the precision-limiting factor. It is clear from Equation (107) that δ_p also depends on the sum of the up and down quark masses, $m_u + m_d = \frac{3}{2}m_d$. It is clear from Equation (44) that Q_{pex} depends on the low-energy value of the fine-structure constant, α. Therefore proton magnetic moment, μ_p, can be calculated from neutron mass, m_n, proton mass, m_p, neutron magnetic moment, μ_n, the sum of the up and down quark masses, $m_u + m_d = \frac{3}{2}m_d$, and the low-energy value of the fine-structure constant, α. However the precision of this calculation, displayed as Equation (119), is limited by the experimental precision of the neutron mangnetic moment, μ_n.

3.3.5. Effective Proton Charge Radii

A recent antineutrino-proton scattering experiment estimated the axial vector form factor of free protons without the need for nuclear theory corrections [51]. In simpler terms, Reference [51] estimated the proton polar axial charge radius, $r_A = 0.73 \pm 0.17$ fm. Figure 1 shows the GSQV proton's effective polar positive-charge radius to be

$$r_A \approx R_p = \frac{\lambda_p}{\sqrt{3}} \approx 0.763 \text{ fm}. \tag{121}$$

Figure 2 shows the GSQV proton's effective polar negative-charge radius to be

$$r_A \approx R_p \sin\phi_{pl} = \lambda_p\sqrt{\tfrac{1}{\sqrt{3}} - \tfrac{1}{4}} \approx 0.756 \text{ fm}. \tag{122}$$

Both of the proton polar axial charge radius estimates, given by Equations (121) and (122), are well inside the experimental range reported in Reference [51]. The research program reported in Reference [51] is ongoing and could potentially falsify the GSQV proton models developed both in this paper and Reference [9].

A key assumption applied when developing the GSQV proton model in Reference [9] was that charge distribution is the radial projection of two concentric uniformly-charged spheres. To a first approximation, this assumption persists in Equations (112) and (114). Deviations from this key assumption are the polar charge-exclusion zones on the GSQV proton's outer apple-shaped charge surface and the relatively tiny δ_p perturbation.

Preprints.org (www.preprints.org) | NOT PEER-REVIEWED | Posted: 14 May 2024 doi:10.20944/preprints202405.0932.v1

Consider a GSQV proton model without charge-exclusion zones and no δ_p perturbation. Radially projecting all charge out to R_{Eo} yields a spherically symmetric charge distribution with electric potential at distance R_{Eo} from the proton center,

$$U(R_{Eo}) = \frac{ke}{R_{Eo}}, \tag{123}$$

where k is Coulomb's constant. Since the GSQV proton model is approximately spherical, electric potential on its outer surface, at average distance

$$r_s = \sqrt[3]{\frac{3}{4\pi}V_{po}} \tag{124}$$

from the proton center, may be approximated by

$$U(r_s) \approx \frac{ke}{r_s}, \tag{125}$$

which implies

$$\frac{U(r_s)}{ke} \approx \frac{1}{r_s}. \tag{126}$$

For a sphere of radius r, surface area, A, and volume V,

$$\frac{rA}{V} = 3. \tag{127}$$

Note that the number 3 is precise in Equation (127). Since a perfect sphere has the minimum surface area to volume ratio for its size, Equation (127) should yield a number greater than 3 for a perturbed sphere. The Appendix of Reference [9] shows how to calculate the surface areas of the volumes defined in Sections 3.1.1 and 3.3.4:

$$A_{ni} = 4\pi R_n^2(\sin\phi_{nl} - \phi_{nl}\cos\phi_{nl}); \tag{128}$$

$$A_{no} = 4\pi R_n^2(\sin\phi_{na} - \phi_{na}\cos\phi_{na}); \tag{129}$$

$$A_{pi} = 4\pi R_p^2(\sin\phi_{pl} - \phi_{pl}\cos\phi_{pl}); \tag{130}$$

$$A_{po} = 2\pi^2 R_p\left(r_{pa} + \frac{2R_p}{\pi}\right) + 2\pi r_{pa}^2. \tag{131}$$

For the unbound GSQV proton model of Section 3.3.4,

$$\frac{r_s A_{po}}{V_{po}} \approx 3.0059. \tag{132}$$

Also note that

$$\frac{r_{pi} A_{pi}}{V_{pi}} \approx 3.0067, \tag{133}$$

Preprints.org (www.preprints.org) | NOT PEER-REVIEWED | Posted: 14 May 2024 doi:10.20944/preprints202405.0932.v1

where

$$r_{pi} = \sqrt[3]{\frac{3}{4\pi} V_{pi}} \approx 0.6810 \text{ fm}. \tag{134}$$

Similarly for the unbound GSQV neutron model, developed in Section 3.1.1,

$$\frac{r_{no} A_{no}}{V_{no}} \approx 3.0791 \text{ and } \frac{r_{ni} A_{ni}}{V_{ni}} \approx 3.1205, \tag{135}$$

where

$$r_{no} = \sqrt[3]{\frac{3}{4\pi} V_{no}} \approx 0.90083 \text{ fm and } r_{ni} = \sqrt[3]{\frac{3}{4\pi} V_{ni}} \approx 0.37856 \text{ fm}. \tag{136}$$

To a first approximation, combining Equations (126) and (132) yields

$$\frac{U(r_s)}{ke} \approx \frac{A_{po}}{3V_{po}}. \tag{137}$$

This implies that a change in outer surface charge area would have approximately three times the effect, on a muon or electron orbital, as a change in charge volume. The charge-exclusion zones of a GSQV proton result in a reduced outer surface charge area,

$$A_{\text{eff}} = A_{po}(1 - Q_{pex}). \tag{138}$$

This is assumed equivalent to an approximately three times smaller effective change in charge volume,

$$V_{\text{eff}} \approx V_{po} \left(1 - \frac{Q_{pex}}{3}\right), \tag{139}$$

with effective charge radius,

$$r_{\text{eff}} = \sqrt[3]{\frac{3}{4\pi} V_{\text{eff}}} \approx \sqrt[3]{\frac{3}{4\pi} V_{po} \left(1 - \frac{Q_{pex}}{3}\right)} \approx 0.8409 \text{ fm}, \tag{140}$$

where Q_{pex} has been calculated by inserting the low-energy fine-structure constant, α, into Equation (44). This estimate is in the middle of the 2022 experimental range of the proton rms charge radius range recommended by the Particle Data Group [5,136], $r_p = 0.8409(4)$ fm. However, since historical experiments to determine proton rms charge radius have been surprisingly variable, this unbound GSQV proton model could be falsified by future experimental estimates of proton rms charge radius.

3.4. Precise Unbound GSQV Neutron Model

Section 3.3.4 showed that proton magnetic moment, μ_p, can be calculated to 7-digit precision from neutron mass, m_n, proton mass, m_p, neutron magnetic moment, μ_n, the sum of the up and down quark masses, $m_u + m_d = \frac{3}{2} m_d$, and the low-energy value of the fine-structure constant, α. The precision-limiting factor is the neutron magnetic moment, μ_n. Since the proton magnetic moment, μ_p, is known to far greater precision than is μ_n, this section will show how to calculate neutron magnetic moment, μ_n, from proton magnetic moment, μ_p, neutron mass, m_n, proton mass, m_p, the sum of the up and down quark masses, $m_u + m_d = \frac{3}{2} m_d$, and the low-energy value of the fine-structure constant, α. The resulting calculation will be substantially more precise than experiment and may place limits on the value of the sum of the up and down quark masses.

The dimensionless quantity, δ_p, will now be used as an adjustable parameter to calculate proton magnetic moment, μ_p, as accurately as the 2018 CODATA value [35,36]. Note that μ_p is the only

Preprints.org (www.preprints.org) | NOT PEER-REVIEWED | Posted: 14 May 2024 doi:10.20944/preprints202405.0932.v1

parameter dependent on δ_p. In particular, Q_{pex} will retain its value calculated from Equation (44). Rearranging Equation (114) by collecting terms to form a quadratic equation in terms of δ_p,

$$a\delta_p^2 + b\delta_p + c = 0, \tag{141}$$

where

$$a = -\left(4-\sqrt{3}\right)^2 \left(1 - Q_{pex}\right) \frac{\lambda_p^3 \mu_p}{4\mu_N}, \tag{142}$$

$$b = \left(4-\sqrt{3}\right)^2 \left(1 - Q_{pex}\right) V_{pi} + 6V_{po}, \tag{143}$$

and

$$c = b - 12V_{po} - a. \tag{144}$$

Applying the quadratic formula,

$$\delta_p = \frac{-b \pm \sqrt{b^2 - 4ac}}{2a} = 2.7353468(15) \times 10^{-4} \text{ and } \approx 2.64, \tag{145}$$

where the 2018 CODATA value of μ_p, displayed as Equation (120), is input to Equation (142). The second solution is unphysical, so $\delta_p = 2.7353468(15) \times 10^{-4}$ provides a calculated proton magnetic moment, μ_p, as precise as the 2018 CODATA value [35,36]. Note that the 2018 CODATA uncertainties in α and μ_p contribute almost equally to the uncertainty in δ_p.

Inverting Equation (107),

$$\delta_n = \frac{4}{3}\left(\frac{m_n}{m_n - \frac{3}{2}m_d}\right)^2 \delta_p. \tag{146}$$

The value $\delta_p = 2.7353468(15) \times 10^{-4}$ will always be used when evaluating Equation (146). Applying the assumption $m_d = 9m_e$ to Equation (146) yields

$$\delta_n = 3.7012807(20) \times 10^{-4}, \tag{147}$$

where the uncertainty is dominated by the uncertainty in δ_p. Applying the assumption $m_d = m_{\pi^\pm} - m_{\pi^0}$ to Equation (146) yields

$$\delta_n = 3.701217(6) \times 10^{-4}, \tag{148}$$

where the uncertainty is dominated by the experimental uncertainty in the pion mass difference–displayed in Equation (105). Inserting the δ_n value, displayed as Equation (147), into Equation (18) yields

$$\mu_n = -1.9130428377(17)\,\mu_N. \tag{149}$$

Inserting the δ_n value, displayed as Equation (148), into Equation (18) yields

$$\mu_n = -1.913042785(5)\,\mu_N. \tag{150}$$

As with Equations (104) and (105), Equations (149) and (150) differ by more than 11 standard deviations. Therefore the different assumptions applied are unlikely to be consistent with each other.

Preprints.org (www.preprints.org) | NOT PEER-REVIEWED | Posted: 14 May 2024 doi:10.20944/preprints202405.0932.v1

The μ_n estimates displayed as Equations (149) and (150) are both consistent with the 2018 CODATA value of μ_n [35,36], displayed as Equation (23). Compared to the experimental uncertainty in the 2018 CODATA value of μ_n, the uncertainties in μ_n displayed in Equations (149) and (150) are respectively about 260 and 90 times lower.

To date, the lowest experimental uncertainty in the neutron magnetic moment was established in 1979 [137]. Reference [138] is a contemporary historical summary of efforts to model, calculate, and measure the neutron magnetic moment. Historically, modeling and calculations have been much less accurate than experiment. However, this paper claims to calculate the neutron magnetic moment substantially better than experiment. Hopefully, this will provide an incentive to design and build new experiments to increase the experimental precision of the neutron magnetic moment.

The experimental uncertainty in the neutron magnetic moment, displayed as Equation (23), may be obtained by varying the sum of the up and down bare quark masses, which were used to derive Equations (107) and (146). Rearranging Equation (107) or (146), and substituting $\frac{3}{2}m_d$ with the more general $m_u + m_d$, yields

$$m_u + m_d = m_n\left(1 - \sqrt{\frac{4\delta_p}{3\delta_n}}\right) = 6.88^{+0.07}_{-0.05}\ \mathrm{MeV/c^2}, \tag{151}$$

where the respective δ_n and δ_p values calculated by Equations (24) and (145) have been applied. Note that the uncertainty in Equation (151) is dominated by the uncertainty in δ_n, and that the uncertainty in δ_n is dominated by the experimental uncertainty in the neutron magnetic moment, μ_n. The experimental uncertainty in $m_u + m_d$, displayed in Equation (101), is almost an order of magnitude larger than that calculated by Equation (151). One way to falsify the unbound GSQV nucleon models developed in this paper would be to experimentally determine $m_u + m_d$ to be statistically inconsistent with Equation (151).

4. Discussion

This paper invokes networks of quantum vacuum waves to develop unbound low-energy nucleon models which calculate several measurable parameters. Using only the proton and neutron mass values as inputs, a physical model is developed that calculates neutron magnetic moment, in the form of Equation (11), to 3-digit precision. If the nuclear magneton was instead defined in terms of the neutron mass, Equation (11) would become an equation that calculates neutron g-factor independently of the nucleon masses. Modifying Equation (11) to Equation (13) possibly illuminates new details of the electron capture process.

Based on quantum networks of standing vacuum waves, this paper develops a model for unbound GSQV nucleon charge arc generation and maintenance. This model establishes a connection between unbound GSQV proton charge structure and the low-energy fine-structure constant. This connection enables the quark charge values to be precisely expressed by Equations (47) and (48) without involving the usual $2/3$ or $1/3$ factors. Noting a numerical coincidence in Equation (72), the low-energy asymptotic value of the fine-structure constant is calculated to 5-digit precision in the form of Equation (75). The quark charge values are then calculated to at least 5-digit precision in the form of Equations (78) and (79).

The unbound GSQV proton model is used to calculate charm quark mass, as Equation (93), and the fraction of the proton momentum carried by intrinsic charm quarks, as Equation (96). This paper proposes a physical model of neutron decay that predicts the W boson mass to be consistent with Equation (100). This prediction is statistically consistent with consensus experimental results. It is shown that the unbound nucleon magnetic moments may be precisely related via the values of the nucleon masses, the sum of the up and down quark masses, and the low-energy fine-structure constant. The most accurate experimental estimate of proton rms charge radius [136] is statistically consistent with the value calculated using Equation (140).

Preprints.org (www.preprints.org) | NOT PEER-REVIEWED | Posted: 14 May 2024 doi:10.20944/preprints202405.0932.v1

This paper's unbound proton and neutron models are shown to be precisely connected via a parameter dependent on neutron mass and the sum of the up and down bare quark masses. Due to this precise connection, and the relatively high experimental precision of proton magnetic moment, unbound nucleon masses, and the low-energy fine-sructure constant, Equations (149) and (150) calculate neutron magnetic moment about two orders of magnitude more precisely than the most accurate experiments to date.

Each of the following would at least partly falsify the unbound low-energy nucleon models developed in this paper:

1. A consensus experimental estimate of charm quark "running" mass [5] that is statistically inconsistent with Equation (93);
2. A consensus experimental estimate of the fraction of the proton momentum carried by intrinsic charm quarks, that is statistically inconsistent with Equation (96), will falsify the assumptions used to derive Equation (94);
3. A consensus experimental estimate of proton rms charge radius that is statistically inconsistent with Equation (140);
4. A consensus experimental estimate of W boson mass, m_W, that is statistically inconsistent with Equation (100), will falsify the assumptions used to derive Equations (107) and (146);
5. A consensus experimental estimate of neutron magnetic moment, μ_n, that is statistically inconsistent with Equation (149), will falsify the assumption expressed by Equation (104);
6. A consensus experimental estimate of neutron magnetic moment, μ_n, that is statistically inconsistent with Equation (150), will falsify the assumption expressed by Equation (105);
7. On the 2 GeV scale, a consensus experimental estimate of the sum of the up and down bare quark masses, $m_u + m_d$, that is statistically inconsistent with Equation (151) will falsify the assumptions used to derive Equations (107) and (146).

Supplementary Materials: The following supporting information can be downloaded at the website of this paper posted on Preprints.org.

Author Contributions: Conceptualization, all authors; methodology, all authors; software, S.V.; validation, all authors; writing—original draft preparation, S.V.; writing—review and editing, all authors; supervision, S.V.; project administration, S.V.; funding acquisition, S.V. and A.O. All authors have read and agreed to the published version of the manuscript.

Funding: During this research project, S.V. was partly supported by UWL Faculty Research Grant 23-01-SV and A.O. was supported by UWL URC grant #35F22. The APC was funded by the authors.

Data Availability Statement: All calculations use publicly available CODATA [35,36] and Particle Data Group [5] data. All calculations were performed using the supplied Excel file.

Conflicts of Interest: The authors declare no conflicts of interest.

Abbreviations

The following abbreviations are used in this manuscript:

EFT	effective field theory
GDH	Gerasimov-Drell-Hearn
GSQV	ground state quantum vortex
QCD	quantum chromodynamics
QED	quantum electrodynamics
QFT	quantum field theory
QGP	quark-gluon plasma
ZIP	zitterbewegung inertial power

Appendix A

The minimum aspect ratio of a smooth paper Möbius band has long been conjectured to be $\sqrt{3}$ [11]. However, a mathematical proof has only recently been proposed [13]. A source of confusion is

Preprints.org (www.preprints.org) | NOT PEER-REVIEWED | Posted: 14 May 2024 doi:10.20944/preprints202405.0932.v1

that Reference [13] explicitly shows how to fold a paper optimal Möbius band with an inside "T" join, but not an outside "T" join. This would not be an issue if the inside "T" join was easy to tape and it was obvious how to refold with an outside "T" join. However, we found neither of these to be without frustration. We note that Figure 1 of Reference [13] is helpful in using paper with a different color on each side. Using such paper greatly helps demonstrate that the folded structure is indeed a Möbius band.

We rediscovered how to fold a paper optimal Möbius band with an outside "T" join. We correctly assumed this to be known classically, which is confirmed by Figure 14.9 of Reference [12]. While the fold lines and instructions in Figure A1 are not fundamentally different to Figure 14.9 of Reference [12], they add clarity and simplicity. Note that the folded optimal paper Möbius band has three layers. A symmetric folding technique, as shown in Reference [13], necessarily results in a symmetric structure–with the join in the middle of the three layers. In contrast, an asymmetric folding technique, as shown by Figure 14.9 of Reference [12] and Figure A1 in this paper, can result in an asymmetric structure–with the join on one of the outer layers.

Young children can easily be taught to fold and tape an optimal paper Möbius band with an outside join. First provide them with any paper rectangle with a $\sqrt{3}$ aspect ratio. None of the fold lines need to be preset. Instruct them to first make the fold labeled "fold forward," in Figure A1, by touching any two of the diagonal corners together. The other two folds then become obvious and can be made in either order. This folding technique is not obvious from the instructions provided in Reference [12]. It is presumably known classically, but we are unaware of this technique being described anywhere in the available literature.

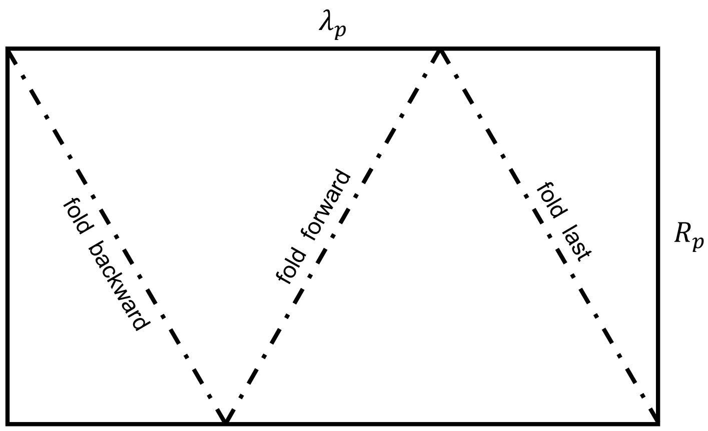

Figure A1. Each of the four charge arcs of an unbound GSQV proton may be continually regenerated by a virtual optimal Möbius band. At each moment in time, at most one inner and one outer charge arc can be regenerated. Therefore an unbound GSQV proton has two virtual optimal Möbius bands. Each optimal Möbius band has aspect ratio $\lambda_p/R_p = \sqrt{3}$, where R_p is the radius of each charge arc. One of several ways to construct a paper optimal Möbius band, with an external "T" join, is to use the fold lines (dash dot) and instructions indicated.

References

1. NNPDF Collaboration. Evidence for intrinsic charm quarks in the proton. *Nature* **2022**, *608*, 483–491.
2. Chen, Y.; Lorcé, C. Nucleon relativistic polarization and magnetization distributions. *Phys. Rev. D* **2023**, *107*.
3. BABAR Collaboration. Study of $e^+e^- \rightarrow p\bar{p}$ via initial-state radiation at BABAR. *Phys. Rev. D* **2013**, *87*, 092005. doi:10.1103/PhysRevD.87.092005.
4. BESIII Collaboration. Oscillating features in the electromagnetic structure of the neutron. *Nature Physics* **2021**, *17*, 1200–1204. doi:10.1038/s41567-021-01345-6.
5. Workman, R.L.; others. Review of Particle Physics. *PTEP* **2022**, *2022*.
6. Peskin, M.; Schroeder, D. *An Introduction to Quantum Field Theory*; Westview Press, 1995.

7. Oerter, R. *The Theory of Almost Everything: The Standard Model, the Unsung Triumph of Modern Physics*; Pi Press: New York, 2006.
8. Sebens, C.T. The fundamentality of fields. *Synthese* **2022**, *200*.
9. Verrall, S.C.; Atkins, M.; Kaminsky, A.; others. Ground State Quantum Vortex Proton Model. *Found. Phys.* **2023**, *53*.
10. Wunderlich, W. Über ein abwickelbares Möbiusband. *Monatshefte für Mathematik* **1962**, *66*, 276–289.
11. Halpern, B.; Weaver, C. Inverting a cylinder through isometric immersions and embeddings. *Trans. Am. Math. Soc* **1977**, *230*, 41–70.
12. Fuchs, D.; Tabachnikov, S. *Mathematical Omnibus: Thirty Lectures on Classic Mathematics*; Vol. 46, AMS, 2007.
13. Schwartz, R.E. The Optimal Paper Moebius Band, 2023, [arXiv:math.MG/2308.12641].
14. G. Amelino-Camelia, L. Freidel, J. Kowalski-Glikman, and L. Smolin. Principle of relative locality. *Phys. Rev. D* **2011**, *84*.
15. Smolin, L. A Real Ensemble Interpretation of Quantum Mechanics. *Found. Phys.* **2012**, *42*, 1239–1261.
16. Cortês, M.; Smolin, L. Quantum energetic causal sets. *Phys. Rev. D* **2014**, *90*.
17. Cortês, M.; Smolin, L. The universe as a process of unique events. *Phys. Rev. D* **2014**, *90*.
18. Cortês, M.; Smolin, L. Spin foam models as energetic causal sets. *Phys. Rev. D* **2016**, *93*.
19. Smolin, L. Quantum Mechanics and the Principle of Maximal Variety. *Found. Phys.* **2016**, *46*, 736–758.
20. Smolin, L. The Dynamics of Difference. *Found. Phys.* **2018**, *48*, 121–134.
21. Smolin, L., Views, variety, and celestial spheres. In *Time and Science - Volume 3: Physical Sciences And Cosmology*; World Scientific, 2023; chapter 9, pp. 239–268.
22. Greensite, J. *An Introduction to the Confinement Problem*; Springer: Germany, 2011.
23. Achenbach, P.; Adhikari, D.; Afanasev, A.; others. The present and future of QCD. *Nuclear Physics A* **2024**, *1047*, 122874. doi:10.1016/j.nuclphysa.2024.122874.
24. Beane, S.R.; Chang, E.; Cohen, S.; Detmold, W.; Lin, H.W.; Orginos, K.; Parreño, A.; Savage, M.J.; Tiburzi, B.C. Magnetic Moments of Light Nuclei from Lattice Quantum Chromodynamics. *Phys. Rev. Lett.* **2014**, *113*.
25. Roberts, C.D.; Richards, D.G.; Horn, T.; Chang, L. Insights into the emergence of mass from studies of pion and kaon structure. *Progress in Particle and Nuclear Physics* **2021**, *120*.
26. Komarov, V.I. Structure of Nucleons and Their Interaction in the Concept of Nonperturbative QCD as a Pressing Issue of 21st-Century Physics. *Phys. Part. Nuclei Lett.* **2022**, *19*, 54–57.
27. V. Bernard, N. Kaiser, and Ulf-G. Meißner. Chiral dynamics in nucleons and nuclei. *Int. J. Mod. Phys. E* **1995**, *4*, 193–344.
28. Zheng, X.; Deur, A.; Kang, H.; others. Measurement of the proton spin structure at long distances. *Nat. Phys.* **2021**, *17*, 736–741.
29. Sulkosky, V.; others. Measurement of the generalized spin polarizabilities of the neutron in the low-Q2 region. *Nat. Phys.* **2021**, *17*, 687–692.
30. Deur, A.; Chen, J.P.; Kuhn, S.E.; others. Experimental study of the behavior of the Bjorken sum at very low Q2. *Physics Letters B* **2022**, *825*.
31. Li, R.; others. Measured proton electromagnetic structure deviates from theoretical predictions. *Nature* **2022**, *611*.
32. Ruth, D.; Zielinski, R.; Gu, C.; others. Proton spin structure and generalized polarizabilities in the strong quantum chromodynamics regime. *Nat. Phys.* **2022**, *18*, 1441–1446.
33. Kegel, S.; others. Measurement of the α-Particle Monopole Transition Form Factor Challenges Theory: A Low-Energy Puzzle for Nuclear Forces? *Phys. Rev. Lett.* **2023**, *130*.
34. Bhattacharya, S.; Cichy, K.; Constantinou, M.; Gao, X.; Metz, A.; Miller, J.; Mukherjee, S.; Petreczky, P.; Steffens, F.; Zhao, Y. Moments of proton GPDs from the OPE of nonlocal quark bilinears up to NNLO. *Phys. Rev. D* **2023**, *108*.
35. Tiesinga, E.; Mohr, P.J.; Newell, D.B.; Taylor, B.N. CODATA Recommended Values of the Fundamental Physical Constants: 2018. *Journal of Physical and Chemical Reference Data* **2021**, *50*, 033105. doi:10.1063/5.0064853.
36. Tiesinga, E.; Mohr, P.J.; Newell, D.B.; Taylor, B.N. CODATA recommended values of the fundamental physical constants: 2018. *Rev. Mod. Phys.* **2021**, *93*, 025010. doi:10.1103/RevModPhys.93.025010.

37. Hagen, W.F. Matter in the form of toroidal electromagnetic vortices. The Nature of Light: What are Photons? VI; Roychoudhuri, C.; Kracklauer, A.F.; Raedt, H.D., Eds. International Society for Optics and Photonics, SPIE, 2015, Vol. 9570.
38. Niehaus, A. Trying an Alternative Ansatz to Quantum Physics. *Found. Phys.* **2022**, *52*.
39. Vassallo, G.; Kovacs, A. The Proton and Occam's Razor. *Journal of Physics Conference Series* **2023**, *2482*, 1–24.
40. Brodsky, S.; Hoyer, P.; Peterson, C.; Sakai, N. The intrinsic charm of the proton. *Physics Letters B* **1980**, *93*, 451–455. doi:10.1016/0370-2693(80)90364-0.
41. Brodsky, S.J.; Peterson, C.; Sakai, N. Intrinsic heavy-quark states. *Phys. Rev. D* **1981**, *23*, 2745–2757. doi:10.1103/PhysRevD.23.2745.
42. The European Muon Collaboration. An experimental limit on the intrinsic charm component of the nucleon. *Physics Letters B* **1982**, *110*, 73–76. doi:10.1016/0370-2693(82)90955-8.
43. NA 3 Collaboration. Experimental J/ψ hadronic production from 150 to 280 GeV/c. *Z. Phys. C - Particles and Fields* **1983**, *20*, 108–116. doi:10.1007/BF01573213.
44. R608 Collaboration. Production of Λ_c with large χ_F at the isr. *Physics Letters B* **1987**, *199*, 304–310. doi:10.1016/0370-2693(87)91379-7.
45. Hobbs, T.J.; Londergan, J.T.; Melnitchouk, W. Phenomenology of nonperturbative charm in the nucleon. *Phys. Rev. D* **2014**, *89*, 074008. doi:10.1103/PhysRevD.89.074008.
46. Vogt, R.; Brodsky, S.; Hoyer, P. Systematics of J/ψ production in nuclear collisions. *Nuclear Physics B* **1991**, *360*, 67–96. doi:10.1016/0550-3213(91)90435-Z.
47. Brodsky, S.J.; Hoyer, P.; Mueller, A.; Tang, W.K. New QCD production mechanisms for hard processes at large x. *Nuclear Physics B* **1992**, *369*, 519–542. doi:10.1016/0550-3213(92)90278-J.
48. LHCb Collaboration. Study of Z Bosons Produced in Association with Charm in the Forward Region. *Phys. Rev. Lett.* **2022**, *128*, 082001. doi:10.1103/PhysRevLett.128.082001.
49. Vogt, R. Limits on intrinsic charm production from the SeaQuest experiment. *Phys. Rev. C* **2021**, *103*, 035204. doi:10.1103/PhysRevC.103.035204.
50. Vogt, R. Energy dependence of intrinsic charm production: Determining the best energy for observation. *Phys. Rev. C* **2022**, *106*, 025201. doi:10.1103/PhysRevC.106.025201.
51. Cai, T.; Moore, M.L.; Olivier, A.; others. Measurement of the axial vector form factor from antineutrino-proton scattering. *Nature* **2023**, *614*, 48–53.
52. Fulling, S.A. Nonuniqueness of Canonical Field Quantization in Riemannian Space-Time. *Phys. Rev. D* **1973**, *7*, 2850–2862.
53. Davies, P.C.W. Scalar production in Schwarzschild and Rindler metrics. *J. Phys. A* **1975**, *8*, 609–616.
54. Unruh, W.G. Notes on black-hole evaporation. *Phys. Rev. D* **1976**, *14*, 870–892.
55. Dewitt, B.S. Quantum gravity: the new synthesis. General Relativity: An Einstein centenary survey; Hawking, S.W.; Israel, W., Eds., 1979, pp. 680–745.
56. Takagi, S. Vacuum Noise and Stress Induced by Uniform Acceleration: Hawking-Unruh Effect in Rindler Manifold of Arbitrary Dimensions. *Progress of Theoretical Physics Supplement* **1986**, *88*, 1–142.
57. Unruh, W.G., Black holes, dumb holes, and entropy. In *Physics meets Philosophy at the Planck Scale*; Cambridge University Press, 2001; pp. 152–173.
58. Matsas, G. The Fulling-Davies-Unruh Effect is Mandatory: The Proton's Testimony. *Int. J. Mod. Phys. D* **2002**, *11*, 1573–1577.
59. Biermann, S.; Erne, S.; Gooding, C.; Louko, J.; Schmiedmayer, J.; Unruh, W.G.; Weinfurtner, S. Unruh and analogue Unruh temperatures for circular motion in 3 + 1 and 2 + 1 dimensions. *Phys. Rev. D* **2020**, *102*.
60. Lochan, K.; Ulbricht, H.; Vinante, A.; Goyal, S.K. Detecting Acceleration-Enhanced Vacuum Fluctuations with Atoms Inside a Cavity. *Phys. Rev. Lett.* **2020**, *125*.
61. Zhang, J.; Yu, H. Entanglement harvesting for Unruh-DeWitt detectors in circular motion. *Phys. Rev. D* **2020**, *102*.
62. Lynch, M.H.; Cohen, E.; Hadad, Y.; Kaminer, I. Experimental observation of acceleration-induced thermality. *Phys. Rev. D* **2021**, *104*.
63. Zhou, Y.; Hu, J.; Yu, H. Entanglement dynamics for Unruh-DeWitt detectors interacting with massive scalar fields: the Unruh and anti-Unruh effects. *J. High Energ. Phys.* **2021**.
64. Zhou, Y.; Hu, J.; Yu, H. Steady-state entanglement for rotating Unruh-DeWitt detectors. *Phys. Rev. D* **2022**, *106*.

65. Anastopoulos, C.; Savvidou, N. Coherences of accelerated detectors and the local character of the Unruh effect. *J. Math. Phys.* **2012**, *53*.
66. Ohanian, H.C.; Ruffini, R. *Gravitation and Spacetime*, third ed.; Cambridge University Press, 2013.
67. Duran, B.; others. Determining the gluonic gravitational form factors of the proton. *Nature* **2023**, *615*.
68. Hansson, J. A simple explanation of the non-appearance of physical gluons and quarks. *Can. J. Phys.* **2002**, *80*, 1093–1097.
69. Coullet, P.; Gil, L.; Rocca, F. Optical vortices. *Opt. Commun.* **1989**, *73*, 403–408.
70. Shen, Y.; Wang, X.; Xie, Z.; others. Optical vortices 30 years on: OAM manipulation from topological charge to multiple singularities. *Light Sci. Appl.* **2019**, *8*.
71. Wan, C.; Cao, Q.; Chen, J.; others. Toroidal vortices of light. *Nat. Photon.* **2022**, *16*, 519–522.
72. Zdagkas, A.; McDonnell, C.; Deng, J.; others. Observation of toroidal pulses of light. *Nat. Photon.* **2022**, *16*, 523–528.
73. Breit, G. An Interpretation of Dirac's Theory of the Electron. *Proceedings of the National Academy of Sciences* **1928**, *14*, 553–559.
74. Schrödinger, E. Über die kräftefreie Bewegung in der relativistischen Quantenmechanik. Sitzungsberichte der Preussischen Akademie der Wissenschaften. Physikali; , 1930; pp. 418–428.
75. Schrödinger, E. Zur Quantendynamik des Elektrons. Sitzungsberichte der Preussischen Akademie der Wissenschaften. Physikali; , 1931; pp. 63–72.
76. Barut, A.O.; Zanghi, N. Classical Model of the Dirac Electron. *Phys. Rev. Lett.* **1984**, *52*, 2009–2012.
77. Hestenes, D. The zitterbewegung interpretation of quantum mechanics. *Found. Phys.* **1990**, *20*, 1213–1232.
78. Greiner, W. *Relativistic Quantum Mechanics*, third ed.; Springer: Germany, 1995.
79. Hestenes, D. Zitterbewegung in quantum mechanics. *Found. Phys.* **2010**, *40*, 1–54.
80. Niehaus, A. A Probabilistic Model of Spin and Spin Measurements. *Found. Phys.* **2016**, *46*, 3–13.
81. Kovács, A.; Vassallo, G.; Di Tommaso, A.O.; Celani, F.; Wang, D. *Maxwell-Dirac Theory and Occam's Razor: Unified Field, Elementary Particles, and Nuclear Interactions*; 2019.
82. Heisenberg, W. Über den Bau der Atomkerne. *Zeitschrift für Physik* **1932**, *77*, 1–11.
83. Wigner, E. On the Consequences of the Symmetry of the Nuclear Hamiltonian on the Spectroscopy of Nuclei. *Phys. Rev.* **1937**, *51*, 106–119.
84. Catillon, P.; Cue, N.; Gaillard, M.J.; others. A Search for the de Broglie Particle Internal Clock by Means of Electron Channeling. *Found. Phys.* **2008**, *38*, 659–664.
85. Wunderlich, C. Trapped ion set to quiver. *Nature* **2010**, *463*, 37–39.
86. Gerritsma, R.; others. Quantum simulation of the Dirac equation. *Nature* **2010**, *463*, 68–71.
87. LeBlanc, L.J.; others. Direct observation of zitterbewegung in a Bose-Einstein condensate. *New J. Phys.* **2013**, *15*.
88. Gaiotto, D.; Kapustin, A.; Seiberg, N.; others. Generalized global symmetries. *J. High Energ. Phys.* **2015**, *172*, 687–692.
89. Córdova, C.; Dumitrescu, T.T.; Intriligator, K.A. Exploring 2-group global symmetries. *J. High Energ. Phys.* **2019**, pp. 1–110.
90. Feynman, R.P. Space-Time Approach to Quantum Electrodynamics. *Phys. Rev.* **1949**, *76*, 769–789.
91. Feynman, R.P. Mathematical Formulation of the Quantum Theory of Electromagnetic Interaction. *Phys. Rev.* **1950**, *80*, 440–457.
92. Feynman, R.P. *QED: The Strange Theory of Light and Matter*; Princeton University Press, 1985.
93. van der Hulst, H.C. Radiogolven uit het wereldruim. *Ned. T. Natuurk.* **1945**, *11*.
94. Shklovski, I.S. A monochromatic radio emission of the galaxy and the possibility of observing it. *Astronomicheski Zhurnal SSSR* **1948**, *26*.
95. Ewen, H.I.; Purcell, E.M. Observation of a line in the galactic radio spectrum. *Nature* **1951**, *168*, 356.
96. Bloch, F.; Siegert, A. Magnetic Resonance for Nonrotating Fields. *Phys. Rev.* **1940**, *57*, 522–527.
97. Levitt, M.H. *Spin Dynamics: Basics of Nuclear Magnetic Resonance*; Wiley, 2001.
98. Peleg, Y.; Pnini, R.; Zaarur, E.; Hecht, E. *Schaum's outline of theory and problems of quantum mechanics*, second ed.; McGraw-Hill: New York, 2010.
99. Guo, X.D.; Dong, L.; Yang, Y.G.; Shan, X.Y.; Zhan, J.M.; Lu, X.H. Detecting Larmor Precession of a Single Spin with a Spin-Polarized Tunneling Current. *Chinese Physics Letters* **2013**, *30*.

100. Gerasimov, S.B. A sum rule for magnetic moments and the damping of the nucleon magnetic moment in nuclei. *Sov. J. Nucl. Phys.* **1966**, *2*.
101. Drell, S.D.; Hearn, A.C. Exact Sum Rule for Nucleon Magnetic Moments. *Phys. Rev. Lett.* **1966**, *16*, 908–911.
102. Drechsel, D.; Tiator, L. The Gerasimov-Drell-Hearn sum rule and the spin structure of the nucleon. *Annual Review of Nuclear and Particle Science* **2004**, *54*, 69–114.
103. Schumacher, M. Polarizability of the nucleon and Compton scattering. *Progress in Particle and Nuclear Physics* **2005**, *55*, 567–646.
104. Helbing, K. The Gerasimov-Drell-Hearn sum rule. *Progress in Particle and Nuclear Physics* **2006**, *57*, 405–469.
105. Adhikari, K.P.; others. Measurement of the Q^2 Dependence of the Deuteron Spin Structure Function g_1 and its Moments at Low Q^2 with CLAS. *Phys. Rev. Lett.* **2018**, *120*.
106. Strakovsky, I.; Širca, S.; Briscoe, W.J.; Deur, A.; Schmidt, A.; Workman, R.L. Single-pion contribution to the Gerasimov-Drell-Hearn sum rule and related integrals. *Phys. Rev. C* **2022**, *105*.
107. Alvarez, L.W. Nuclear *K* Electron Capture. *Phys. Rev.* **1937**, *52*, 134–135. doi:10.1103/PhysRev.52.134.
108. Alvarez, L.W. Electron Capture and Internal Conversion in Gallium 67. *Phys. Rev.* **1938**, *53*, 606–606. doi:10.1103/PhysRev.53.606.
109. Alvarez, L.W. The Capture of Orbital Electrons by Nuclei. *Phys. Rev.* **1938**, *54*, 486–497. doi:10.1103/PhysRev.54.486.
110. Griffiths, D. *Introduction to Elementary Particles*; Wiley, 2008.
111. Pourshahian, S. Mass Defect from Nuclear Physics to Mass Spectral Analysis. *Journal of The American Society for Mass Spectrometry* **2017**, *28*, 1836–1843. doi:10.1007/s13361-017-1741-9.
112. Larmor, J. LXIII. On the theory of the magnetic influence on spectra; and on the radiation from moving ions. *The London, Edinburgh, and Dublin Philosophical Magazine and Journal of Science* **1897**, *44*, 503–512.
113. Ren, H.; Weinberg, E.J. Radiation from a moving scalar source. *Phys. Rev. D* **1994**, *49*, 6526–6533. doi:10.1103/PhysRevD.49.6526.
114. Cozzella, G.; Fulling, S.A.; Landulfo, A.G.S.; Matsas, G.E.A. Uniformly accelerated classical sources as limits of Unruh-DeWitt detectors. *Phys. Rev. D* **2020**, *102*, 105016. doi:10.1103/PhysRevD.102.105016.
115. Portales-Oliva, F.; Landulfo, A.G.S. Classical and quantum reconciliation of electromagnetic radiation: Vector Unruh modes and zero-Rindler-energy photons. *Phys. Rev. D* **2022**, *106*, 065002. doi:10.1103/PhysRevD.106.065002.
116. Lynch, M.H.; Ievlev, E.; Good, M.R.R. Accelerated electron thermometer: observation of 1D Planck radiation. *Progress of Theoretical and Experimental Physics* **2023**, *2024*, 023D01. doi:10.1093/ptep/ptad157.
117. Vacalis, G.; Higuchi, A.; Bingham, R.; Gregori, G. Classical Larmor formula through the Unruh effect for uniformly accelerated electrons. *Phys. Rev. D* **2024**, *109*, 024044. doi:10.1103/PhysRevD.109.024044.
118. Ievlev, E.; Good, M.R.R. Thermal Larmor Radiation. *Progress of Theoretical and Experimental Physics* **2024**, *2024*, 043A01. doi:10.1093/ptep/ptae042.
119. Singh, T.P. Quantum gravity effects in the infrared: a theoretical derivation of the low-energy fine structure constant and mass ratios of elementary particles. *Eur. Phys. J. Plus* **2022**, *137*.
120. Diez, M.; Alkofer, R.; Kohlfürst, C. Identifying time scales in particle production from fields. *Physics Letters B* **2023**, *844*.
121. Sen, D. The Uncertainty Relations in Quantum Mechanics. *Current Science* **2014**, *107*, 203–218.
122. McLerran, L.; Tribedy, P. Intrinsic fluctuations of the proton saturation momentum scale in high multiplicity p+p collisions. *Nuclear Physics A* **2016**, *945*, 216–225. doi:10.1016/j.nuclphysa.2015.10.008.
123. Pvoh, B.; Scholz, C.; Rith, K.; Zetsche, F. *Particles and Nuclei*; Springer, 2008.
124. Leader, E.; Anselmino, M. A crisis in the parton model: Where, oh where is the proton's spin? *Z. Phys. C* **1988**, *41*, 239–246.
125. European Muon Collaboration. A measurement of the spin asymmetry and determination of the structure function g_1 in deep inelastic muon-proton scattering. *Phys. Lett. B* **1988**, *206*, 364–370.
126. Hansson, J. The "Proton Spin Crisis" — a Quantum Query. *Prog. Phys.* **2010**, *3*, 51–52.
127. Heyde, K. *Basic Ideas and Concepts in Nuclear Physics: An Introductory Approach*, third ed.; Taylor & Francis, 2004.
128. Conti, M.; Eriksson, L. Physics of pure and non-pure positron emitters for PET: a review and a discussion. *EJNMMI Physics* **2016**, *3*. doi:10.1186/s40658-016-0144-5.

129. de Blas, J.; Ciuchini, M.; Franco, E.; Goncalves, A.; Mishima, S.; Pierini, M.; Reina, L.; Silvestrini, L. Global analysis of electroweak data in the Standard Model. *Phys. Rev. D* **2022**, *106*, 033003. doi:10.1103/PhysRevD.106.033003.
130. ATLAS Collaboration. Measurement of the W-boson mass and width with the ATLAS detector using proton-proton collisions at $\sqrt{s} = 7$ TeV, 2024, [arXiv:hep-ex/2403.15085].
131. Fazzini, T.; Fidecaro, G.; Merrison, A.W.; Paul, H.; Tollestrup, A.V. Electron Decay of the Pion. *Phys. Rev. Lett.* **1958**, *1*, 247–249. doi:10.1103/PhysRevLett.1.247.
132. Crawford, J.F.; Daum, M.; Frosch, R.; Jost, B.; Kettle, P.R.; Marshall, R.M.; Wright, B.K.; Ziock, K.O.H. Precision measurement of the pion mass difference $m_{\pi^-} - m_{\pi^0}$. *Phys. Rev. D* **1991**, *43*, 46–58. doi:10.1103/PhysRevD.43.46.
133. Heald, M. Where is the "Wien peak"? *Am. J. Phys.* **2003**, *71*. doi:https://doi.org/10.1119/1.1604387.
134. Fromerth, M.; Kuznetsova, I.; Labun, L.; Letessier, J.; Rafelski, J. From Quark-Gluon Universe to Neutrino Decoupling: 200 < T < 2 MeV. *Acta Phys. Pol. B* **2012**, *43*. doi:10.5506/APhysPolB.43.2261.
135. Schneider, G.; Mooser, A.; Bohman, M.; Schön, N.; Harrington, J.; Higuchi, T.; Nagahama, H.; Sellner, S.; Smorra, C.; Blaum, K.; Matsuda, Y.; Quint, W.; Walz, J.; Ulmer, S. Double-trap measurement of the proton magnetic moment at 0.3 parts per billion precision. *Science* **2017**, *358*, 1081–1084. doi:10.1126/science.aan0207.
136. Antognini, A.; others. Proton Structure from the Measurement of $2S - 2P$ Transition Frequencies of Muonic Hydrogen. *Science* **2013**, *339*, 417–420.
137. Greene, G.L.; Ramsey, N.F.; Mampe, W.; Pendlebury, J.M.; Smith, K.; Dress, W.B.; Miller, P.D.; Perrin, P. Measurement of the neutron magnetic moment. *Phys. Rev. D* **1979**, *20*, 2139–2153. doi:10.1103/PhysRevD.20.2139.
138. Sharda, A. Calculation and modeling of the neutron's magnetic moment. Master's thesis, University of Tennessee, 2021.